Supplementary Information

Electron-Withdrawing Chemistry Drives Ultrafast-Charging Interphases for Sodium-ion Batteries

Fuqiang Li[1], Zhichao Li[1], Dongfang Dong[2], Cheng Yang[2]*, Yu Liu[2]*, Yanfeng Gao[1,3]*
[1]School of College of Science, Shanghai University
Shanghai 200444, China
[2]Shanghai Institute of Ceramics, Chinese Academy of Sciences
Shanghai 200050, China
[3]State Key Laboratory of Advanced Refractories, Shanghai University, Shanghai, 200444, China
*Corresponding author E-mail address:
yfgao@shu.edu.cn
yuliu@mail.sic.ac.cn
yangcheng@mail.sic.ac.cn

Table of Contents

Methods

Electrolytes and electrode synthesis. All the carbonate electrolyte were purchased from Aladdin and purified by distillation under vacuum; the solvents were dried three times by 4 Å molecular sieves before the preparation of electrolytes. The electrolyte was composed of 1 M sodium bis(fluorosulfonyl)imide (NaFSI) dissolved in a mixture of ethylene carbonate (EC), dimethyl carbonate (DMC), and a co-solvent of diethyl carbonate (nonF-DEC)/ethyl trifluoroethyl carbonate (semF-DEC)/and bis(trifluoroethyl) carbonate (fulF-DEC) in a volume ratio of 25:65:10. All electrolytes were prepared by utilizing an electronic balance and pipette in the glove box. HC materials were provided by Kuraray China Co., Ltd. HC, Super P (TIMCAL, Switzerland), and carboxymethylcellulose sodium (Wealthy, China) were mixed in a 7:2:1 weight ratio and ball-milled in a high-energy mechanical mill (BYT, XGB2, China) with the rotation speed of 450 rpm for 4 h to form a homogeneous slurry. Then, the slurry was scraped on the Al foil (Canrd, China) to prepare electrodes with a thickness of 250 μm. Then, the Al foil was dried at 100 °C for 9 h in a vacuum atmosphere. The foil was cut into electrode sheets with a diameter of 14 mm for later use. The NFPP was supported by Jiangsu Benan Technology Co., Ltd, and was prepared by mixing 80% active material, 10% conductive carbon black (acetylene black), and 10% poly-vinylidene difluoride (PVDF, dissolved in N-methylpyrrolidone), and the paste is also applied on to Al foil, and was dried at 100 °C for 9 h in a vacuum atmosphere. The mass loading of HC anode and NFPP cathode were about 2.0 mg cm^{-2} and 3 mg cm^{-2}, respectively. The HC||NFPP pouch cells are designed with a capacity of 1 Ah. The active material loading of the negative and positive electrodes are around 120 and 320 g m^{-2}, respectively, and the N/P ratio is 1.2. The pouch cell is filled with the liquid electrolyte at a ratio of 9 g Ah^{-1}. The prismatic full cell is designed with a capacity of 52 Ah. The active material loading of the negative and positive electrodes are around 179 and 380 g m^{-2}, respectively, and the N/P ratio is 1.32, and is filled with the liquid electrolyte (410g).

Characterizations. The moisture content of the electrolyte was measured by Karl Fischer titrator (AKF-CH6). Fourier transform infrared spectroscopy (FTIR) spectra were tested by the Nicolet iS10 FTIR spectrometer in the range of 4000 to 400 cm^{-1}. The number of scans was 32 and the resolution for FTIR measurements was 4 cm^{-1}. All FTIR spectra were analyzed by Origin software. All ^{23}Na and ^{19}F nuclear magnetic resonance (NMR) spectra were tested by NMR spectrometer (Bruker Ascend). The surface morphology of cycled HC anodes was observed by transmission electron microscope (TEM, TEOL-2100F) and atomic force microscopy (AFM, Bruker-Dimension Icon). The solid electrolyte interphase (SEI) was performed by X-ray photoelectron spectroscopy (XPS, Thermo Kalpha) and Time of Flight Secondary Ion Mass Spectrometry (TOF-SIMS, IONTOF TOF.SIMS 5). Contact angle measurements of the electrolytes on the electrode were performed by a contact angle measurement system (CA100D, Yinnuo). Electrochemical impedance spectroscopy (EIS), linear sweeping voltammetry (LSV) and cyclic voltammetry (CV) were performed on the electrochemical workstation (AUTOLAB). Galvanostatic

charge/discharge (GCD) cycling tests were carried out on the LAND CT2100A.

Electrochemical Measurements. CR2032 coin cells were fabricated by using HC as anode, glass fiber (~650 μm) as separator, and Na tablet as anode. The electrolytes were those prepared above. The coin cells were assembled in an argon-filled glove box (H_2O and O_2 < 0.1 ppm). The typical galvanostatic electrochemical tests were carried out in a LANHE test equipment. The EIS, LSV and CV were tested by an electrochemical workstation (AUTOLAB). The AC signal ranging from 0.01 Hz to 100 kHz was used for all the EIS tests, and the EIS tests at different cycle numbers were performed in the fully discharged state. The sodium tablets and Al foil were used as the counter, reference and working electrodes, respectively, for LSV test with a scanning rate of 5 mV s^{-1}.

GITT test was conducted and the diffusion coefficient was calculated based on the equation [1]:

$$D = \frac{4}{\pi}\left(\frac{m_B V_M}{M_B S}\right)^2\left(\frac{\Delta E_s}{\Delta E_\tau}\right)^2\frac{1}{\tau}$$

where m_B, V_M and M_B are the mass, molar volume and molar mass of HC, respectively. τ is the relaxation time, S is the electrode area, ΔE_S is the voltage change caused by pulse (3600 s), $\Delta E_{\square}$ is the voltage change caused by charging and discharging (600 s).

Randles-Sevcik plots showing the linear relationship between peak current and the square root of scan rate and the diffusion coefficient was calculated based on the equation[2]:

$$I_p = 2.69 \times 10^5 n^{3/2} A D^{1/2} C v^{1/2}$$

where I_p is the peak current, n is the number of electrons transferred, A is the electrode area, D is the diffusion coefficient, C is the concentration, and v is the scan rate.

The temperature dependence of the interfacial resistance was analyzed using an Arrhenius relationship [3]:

$$\ln\left(\frac{T}{R}\right) = -\frac{E_a}{R}\cdot\frac{1}{T} + \ln\left(\frac{1}{R_0}\right)$$

where R is the interfacial resistance, R_0 is a pre-exponential factor, E_a is the activation energy, R is the gas constant (8.314 J $mol^{-1}K^{-1}$), and T is the absolute temperature.

The activation energy was obtained from the linear fitting of ln(T/R) versus 1/T.

Theoretical Calculations. Quantum chemistry calculations were conducted using the Gaussian 09 package at B3LYP/6-311+ G (d, p) level of theory to optimize molecular structures of EC, DMC, nonF-DEC, semF-DEC, fulF-DEC, Na^+-solvent and FSI^--solvent complexes and calculate the molecular orbital energy and binding energy. The ESP mapping was acquired by the further calculation of Gaussian check files [4-8]. MD simulations for the electrolyte structures were conducted by using the

GROMACS package with the GROMOS96 G54A7 force field. The MD parameters for Na^+ were in the built-in force field parameters. Packmol was applied to generate initial coordinates for MDs with prearranged concentrations [9-10]. A cutoff radius of 1 nm was set for short-ranged van der Waals interactions and electrostatic interactions in real space interactions. The particle-mesh Ewald (PME) summation method was employed to handle long range electrostatic interactions in reciprocal space with an interpolation order of 4 and a Fourier grid spacing of 0.16 nm. The systems were equilibrated in NVT ensemble using the V-rescale barostat for 4 ns to maintain a temperature of 300 K. Another 100 ns production run in NPT ensemble at 300 K was conducted finally. A time step of 1 fs was used for all simulations [11]. The results of MD simulations are produced by VMD software [12]. The binding energy (E) of Na^+/FSI^- of solvents was calculated with the equation following $E=E_{ion\text{-}solvent} - E_{ion} - E_{solvent}$, $E_{ion\text{-}solvent}$, E_{ion} and $E_{solvent}$ represent the total energy of Na^+/FSI^--solvent complex, the single Na^+/FSI^- and the isolated solvent molecule, respectively. Additionally, Multiwfn 3.8 was employed to visualize the optimized structures or to get reduced density gradient (RDG) for analyzing the noncovalent interactions with visualizations by VMD [13-14].

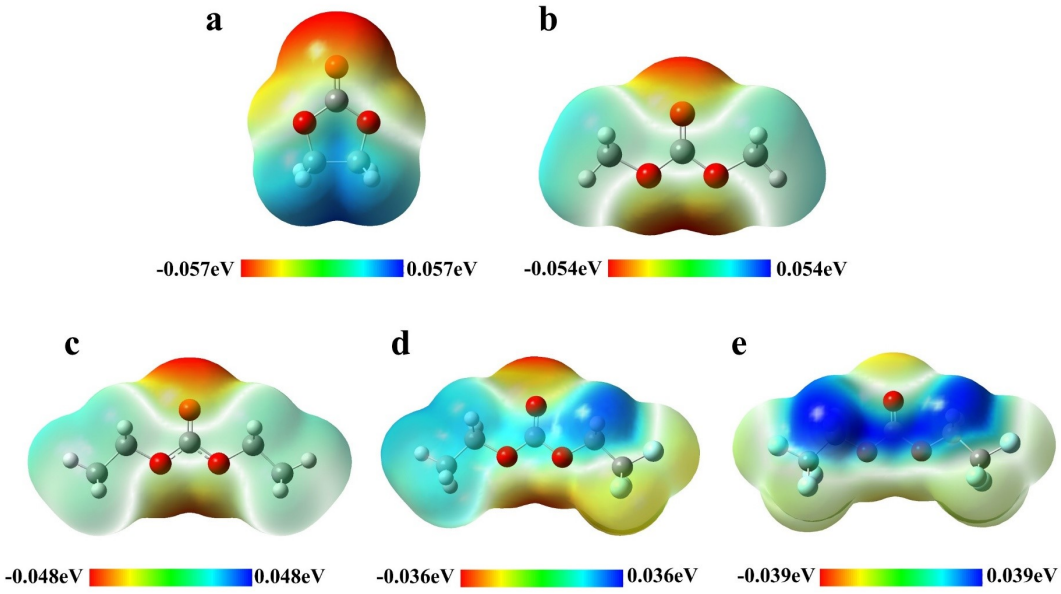

Fig. S1 The ESP maps of EC, DMC, nonF-DEC, semF-DEC and fulF-DEC.

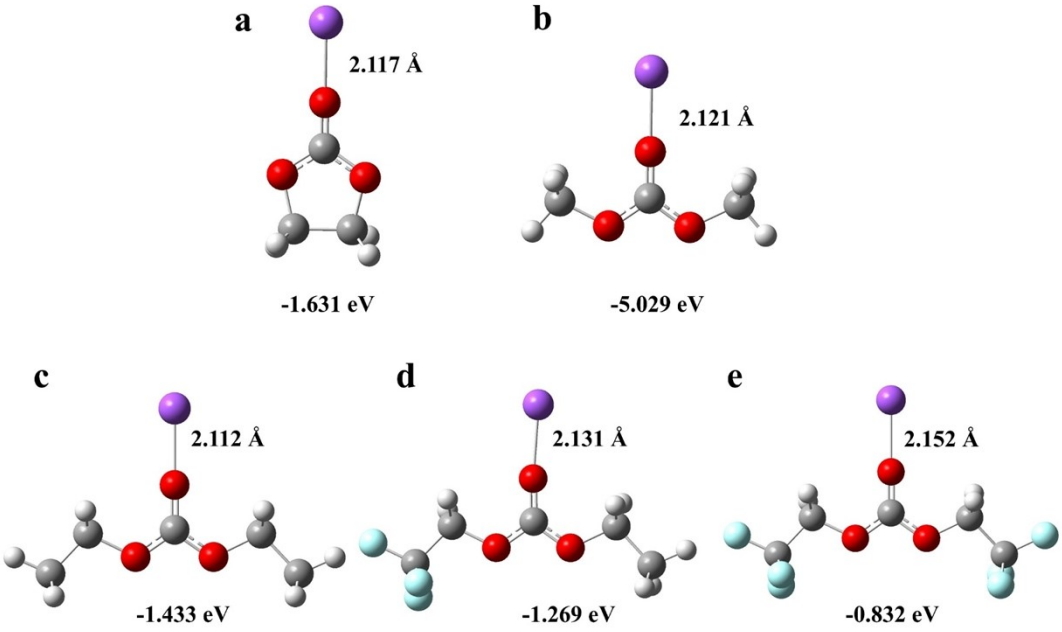

Fig. S2 Calculated coordination structures and binding energies of Na^+–solvents. (a) EC-Na^+, (b) DMC-Na^+, (c) nonF-DEC -Na^+, (d) semF-DEC-Na^+, (e) fulF-DEC-Na^+.

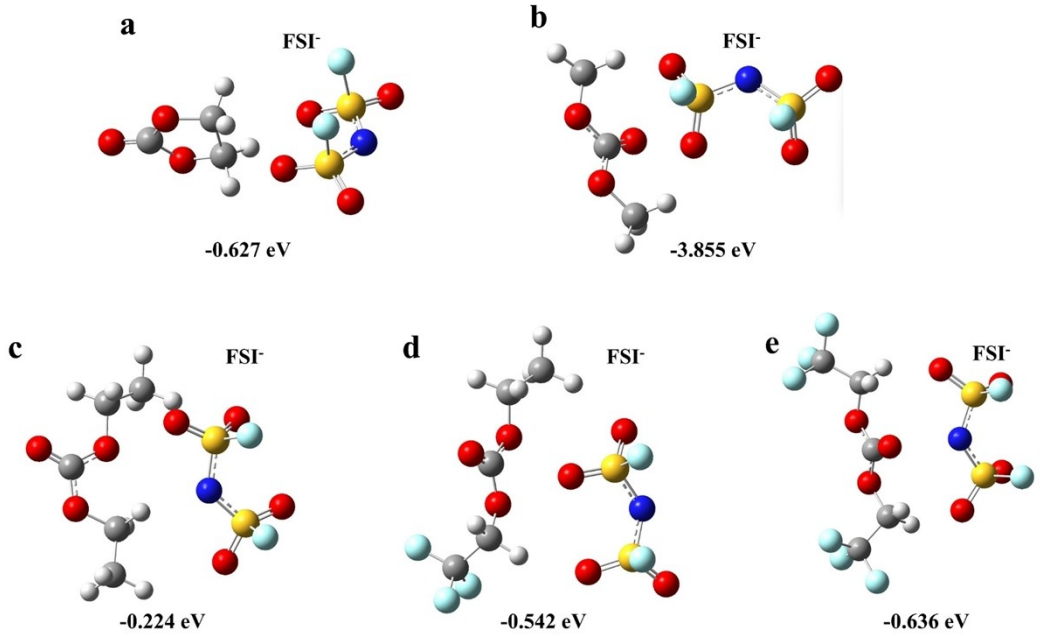

Fig. S3 Calculated binding structure and binding energy of FSI^-–solvents. (a) EC-FSI^-, (b) DMC-FSI^-, (c) nonF-DEC-FSI^-, (d) semF-DEC-FSI^-, (e) fulF-DEC-FSI^-.

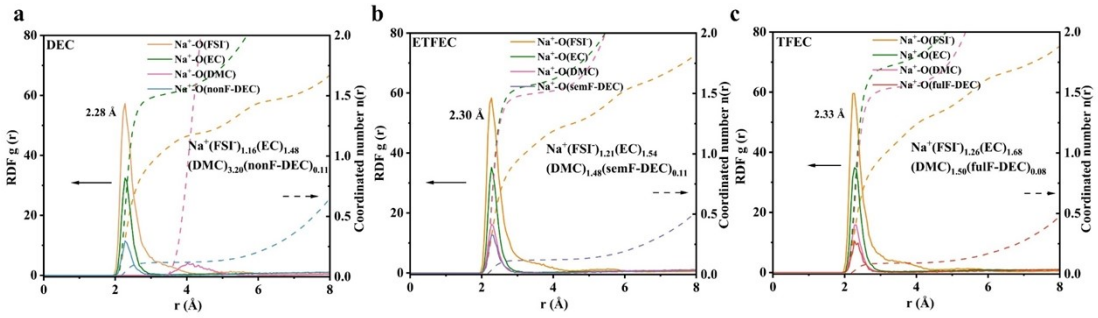

Fig. S4 Na^+ RDFs and CN in different electrolytes.

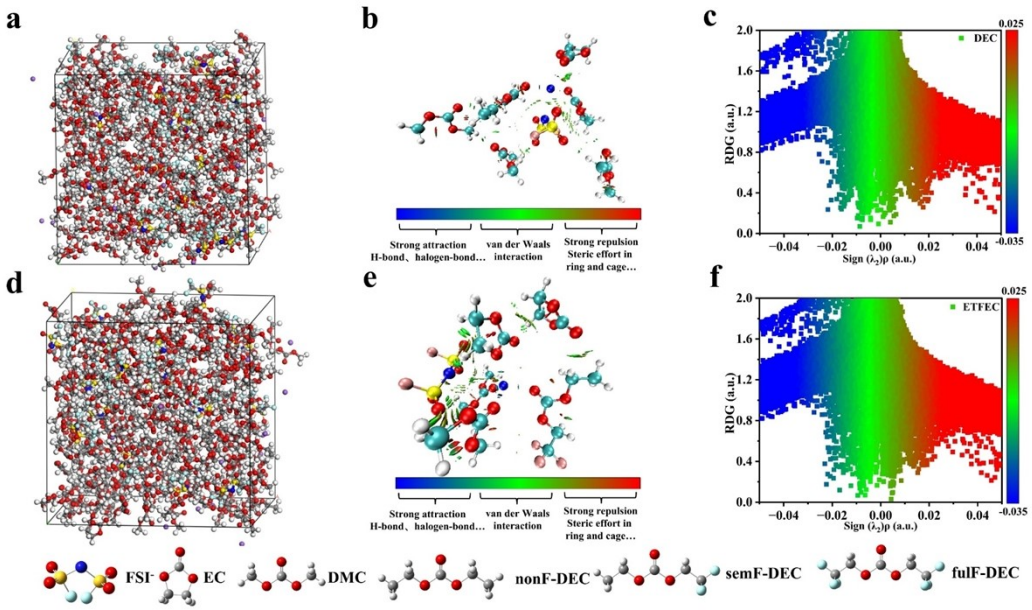

Fig. S5 (a, b, c) Molecular dynamic (MD) simulation trajectory, IGM and RDG diagrams of DEC electrolyte. (d, e, f) Molecular dynamic (MD) simulation trajectory, IGM and RDG diagrams of ETFEC electrolyte.

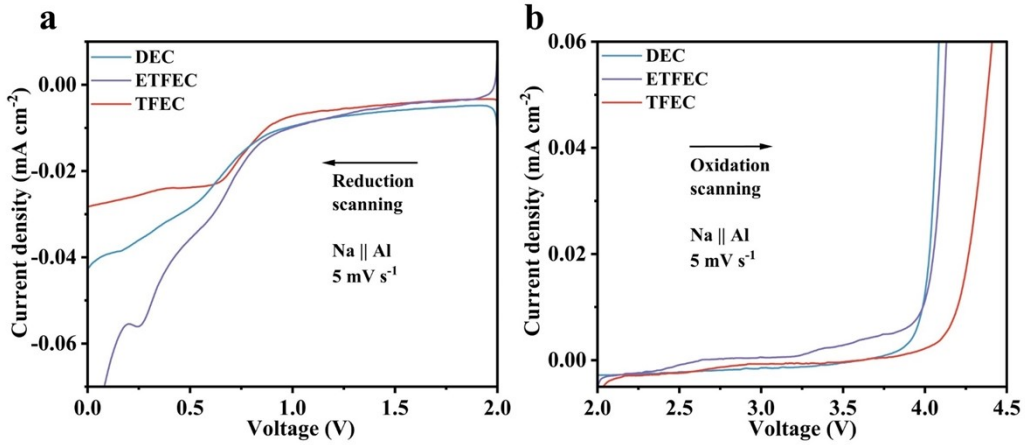

Fig. S6 The electrochemical window of electrolytes at (a) reduction and (b) oxidation process.

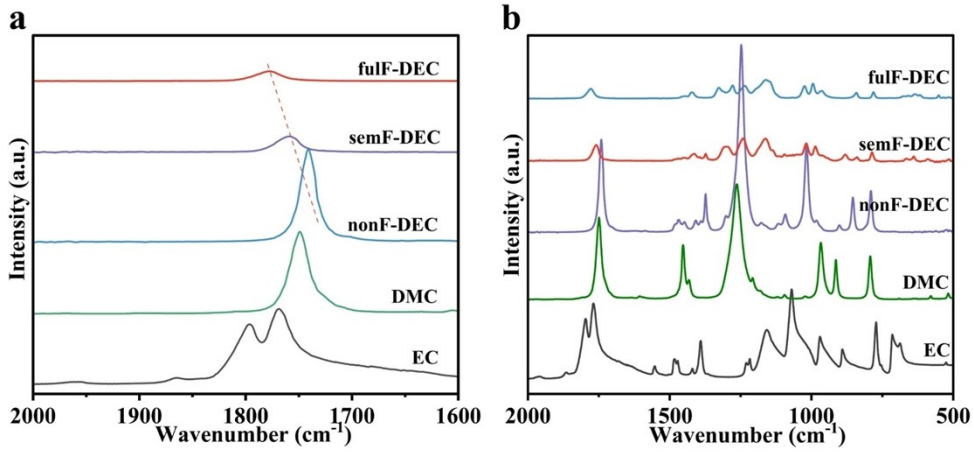

Fig. S7 FTIR spectra of the electrolytes and several pure solvents.

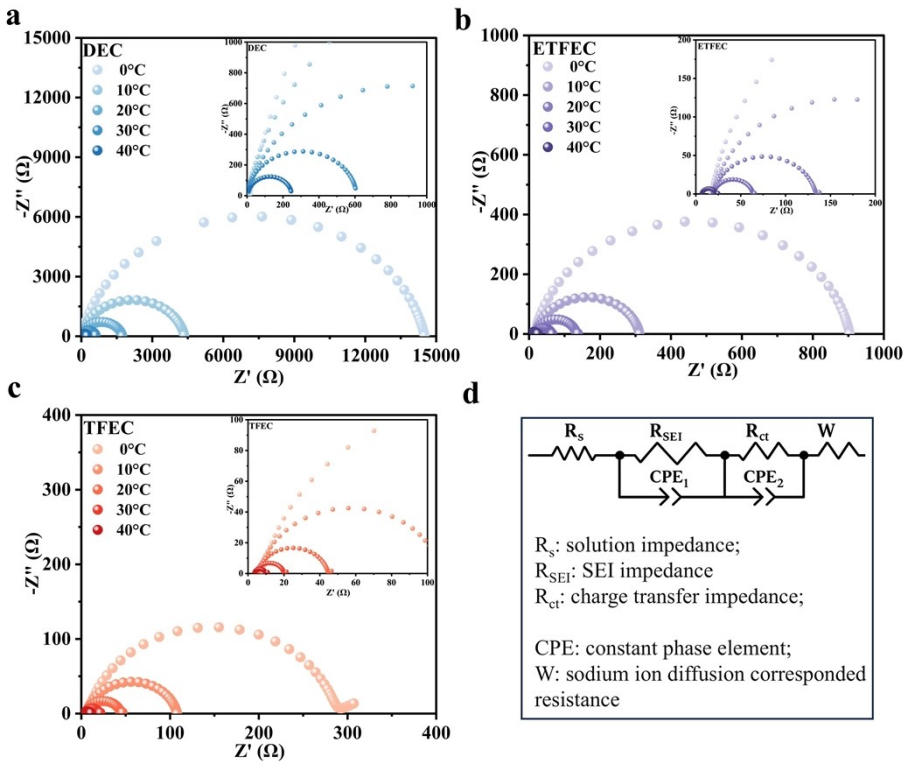

Fig. S8 Nyquist plots of Na||Na symmetric batteries with (a) DEC, (b) ETFEC and (c) TFEC electrolyte from 0 °C to 40 °C. (d) The equivalent circuit of the above impedance fitting.

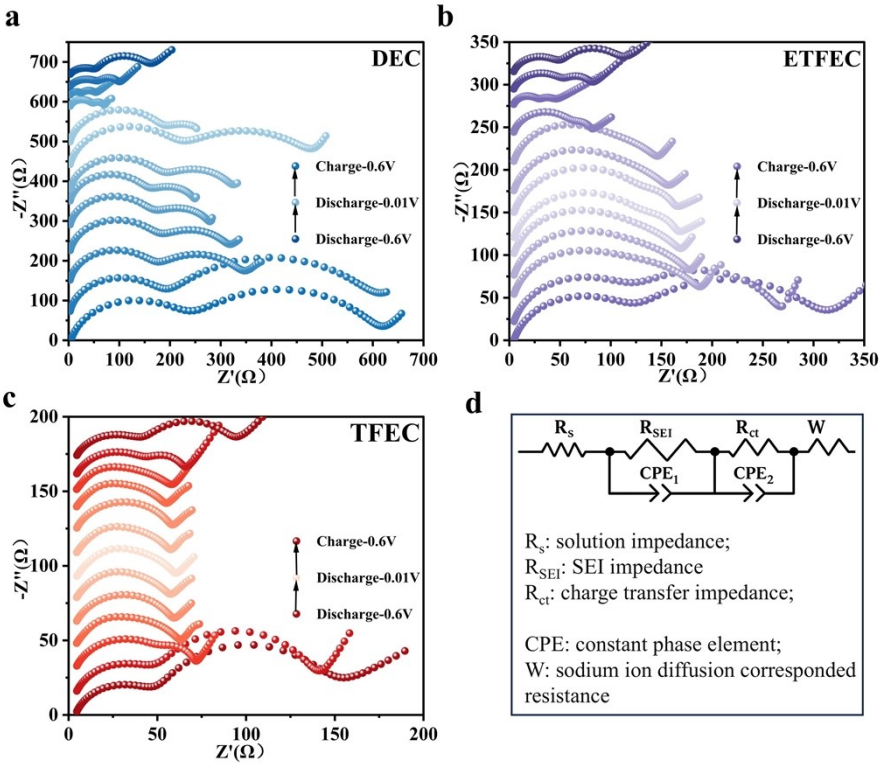

Fig. S9 The in-situ electrochemical impedances of (a) DEC, (b) ETFEC and (C) TFEC electrolytes for the first cycle.

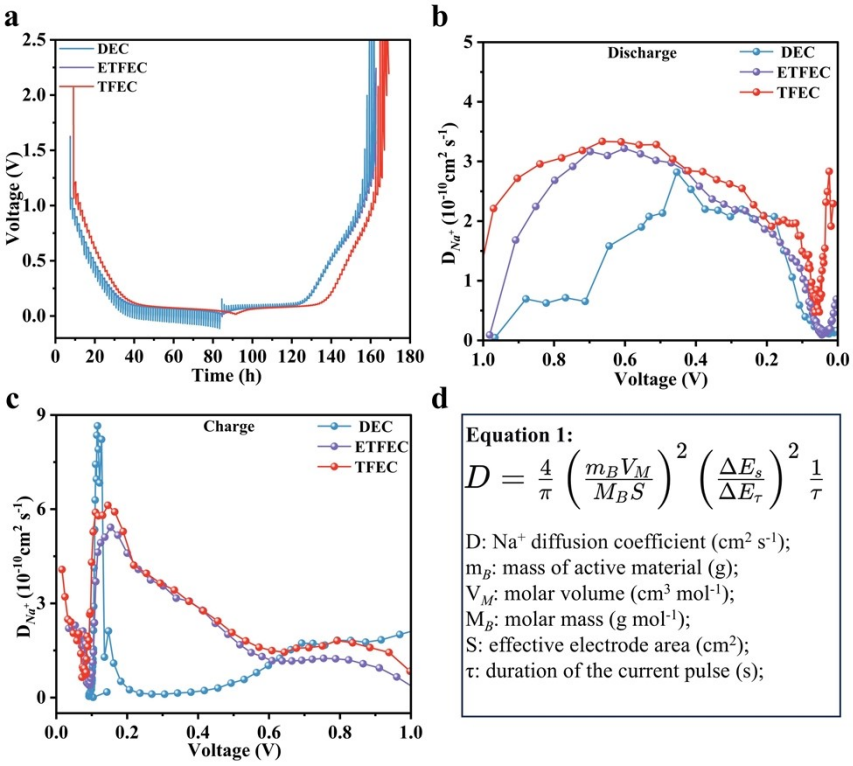

Fig. S10 The galvanostatic intermittent titration test of DEC, ETFEC and TFEC cells.

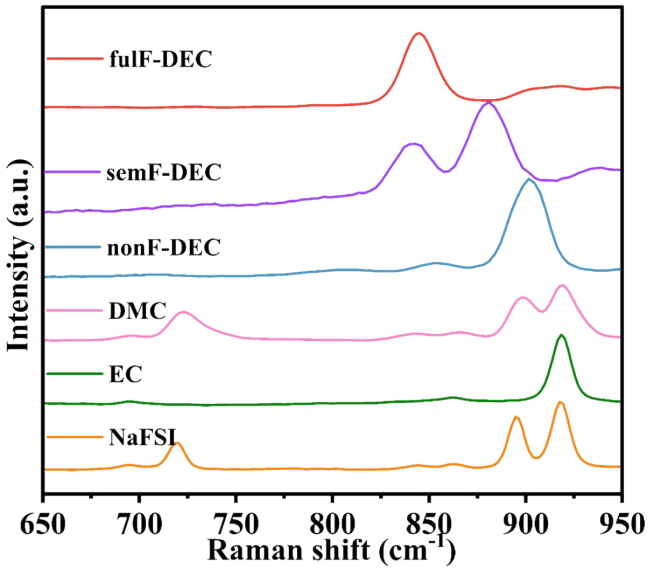

Fig. S11 Raman spectra of several pure solvents.

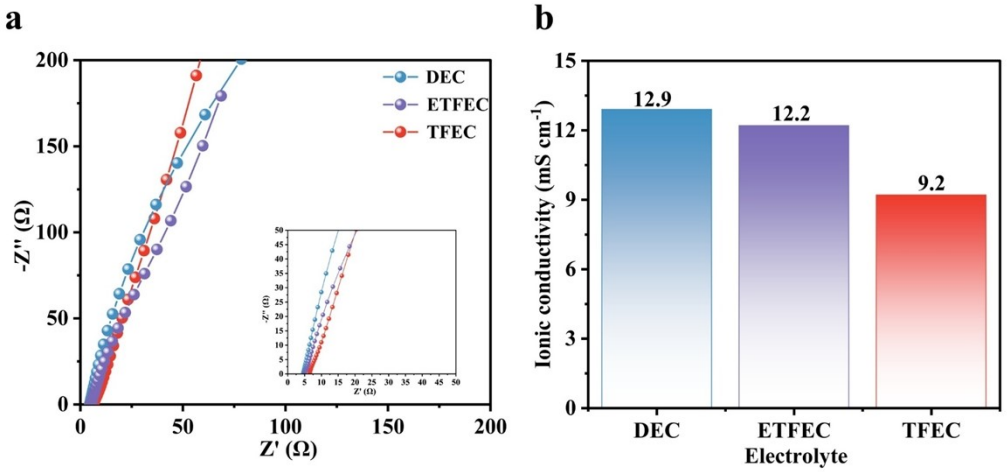

Fig. S12 The ionic conductivities of the different electrolytes.

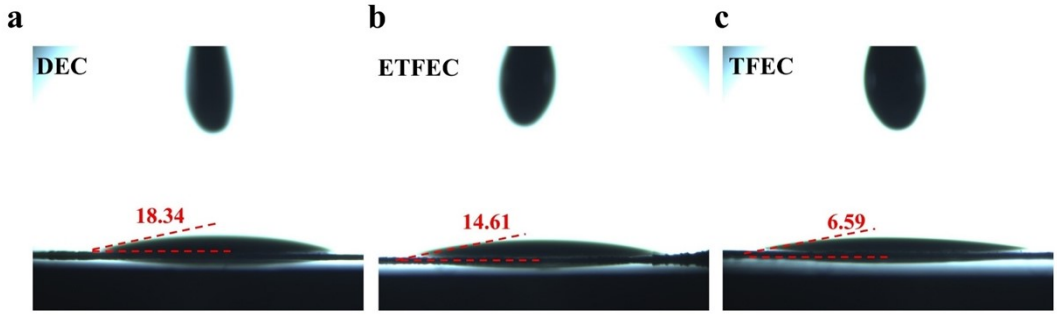

Fig. S13 Contact angle measurements of different electrolytes.

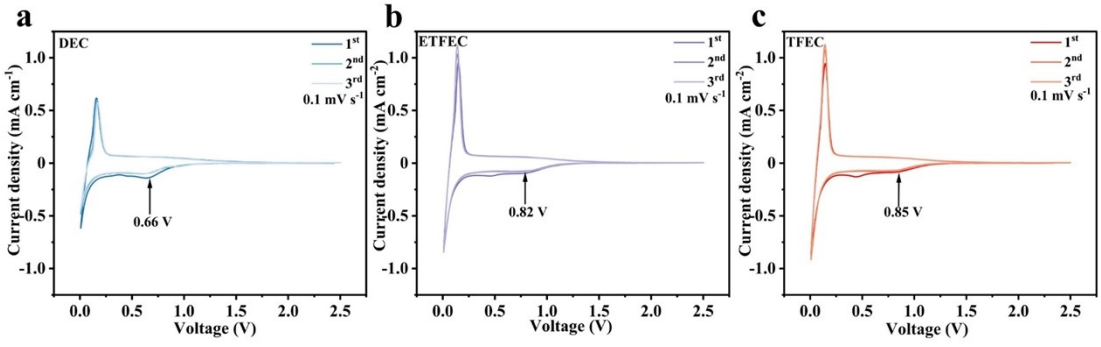

Fig. S14 The cyclic voltammogram curves of the (a) DEC, (b) ETFEC and (c) TFEC electrolytes during three cycles.

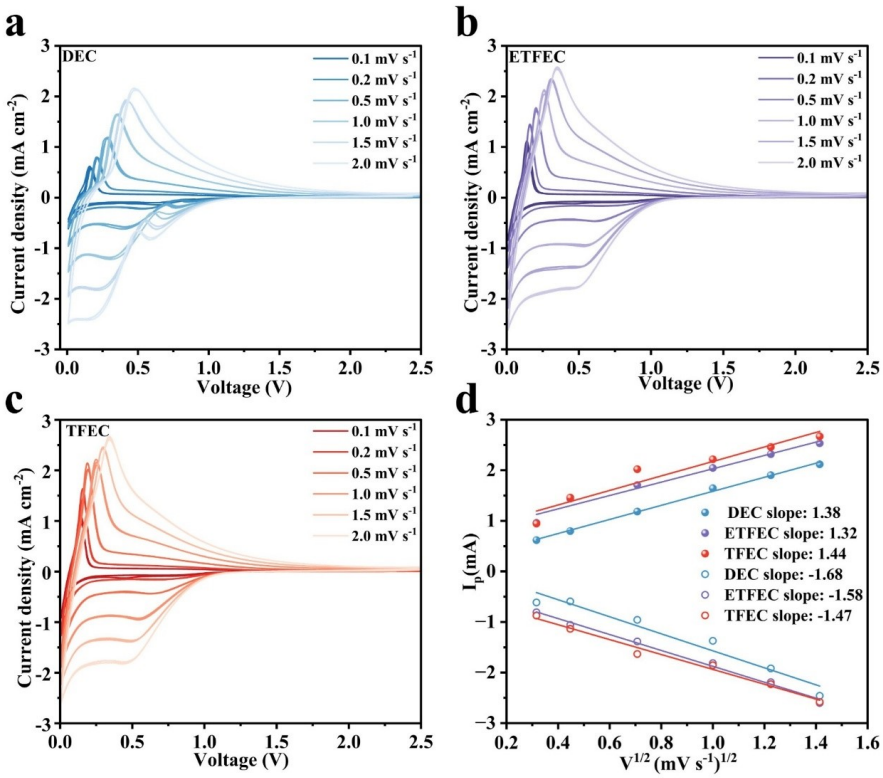

Fig. S15 The cyclic voltammogram curves of the (a) DEC, (b) ETFEC and (c) TFEC electrolytes with different scan rates. (d) The linear fitting results for the absolute peak current intensity (I_p) as a function of the square root of the scan rate ($v^{1/2}$) of different electrolytes.

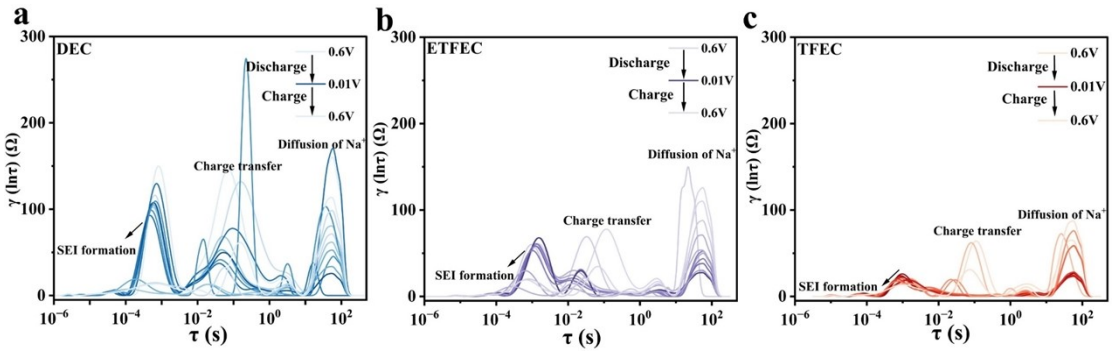

Fig. S16 The DRT curves of HC||Na cells after the first charge/discharge cycle with (a) DEC, (b) ETFEC and (c) TFEC electrolytes.

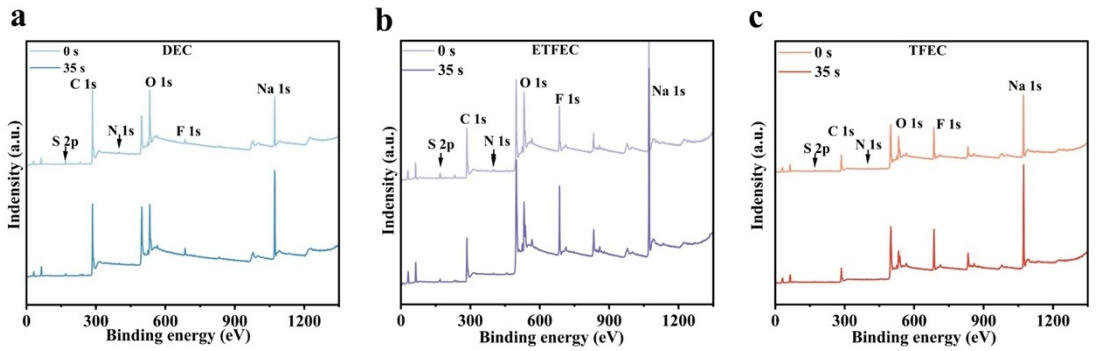

Fig. S17 The broad XPS spectra in the (a) DEC, (b) ETFEC and (C) TFEC electrolytes.

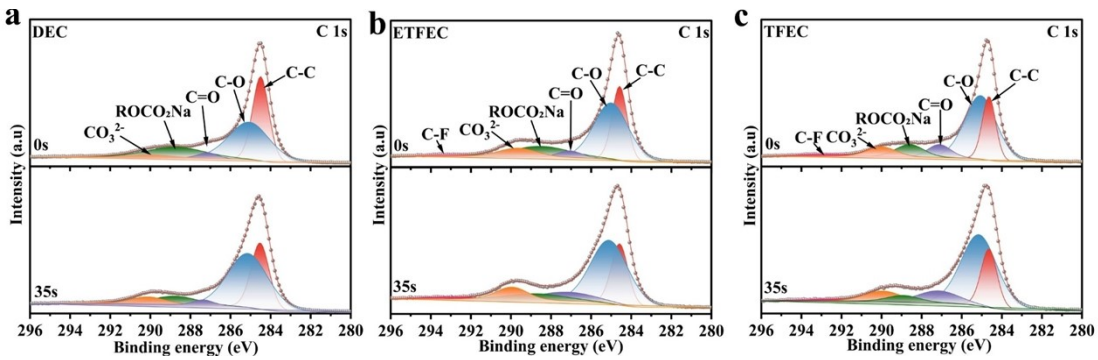

Fig. S18 XPS spectra C 1s of HC anodes cycling in different electrolytes after 10 cycles.

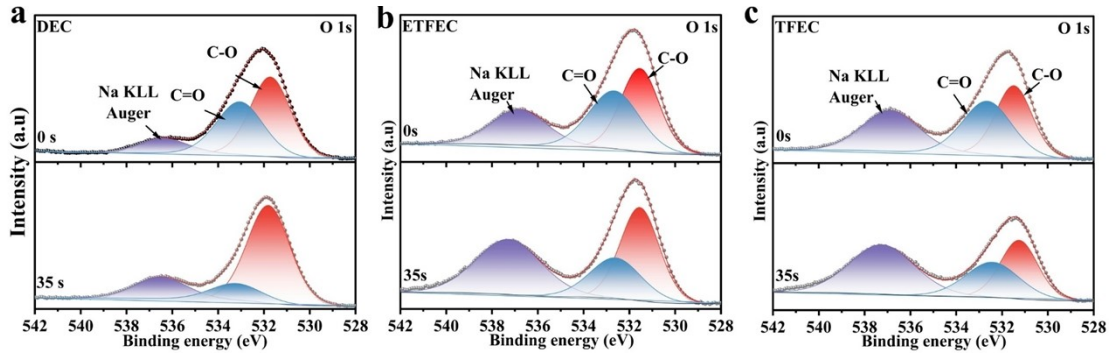

Fig. S19 XPS spectra O 1s of HC anodes cycling in different electrolytes after 10 cycles.

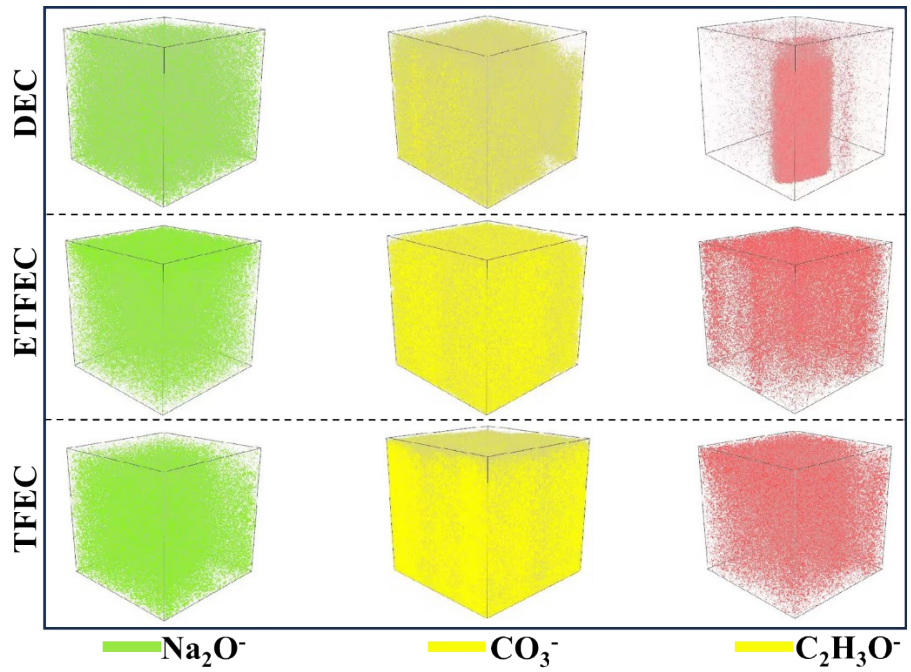

Fig. S20 The 3D views of Na_2O^-, F^-, CO_3^- and $C_2H_3O^-$ ionic fragments in the TOF-SIMS volumes of electrodes in DEC, ETFEC and TFEC electrolytes.

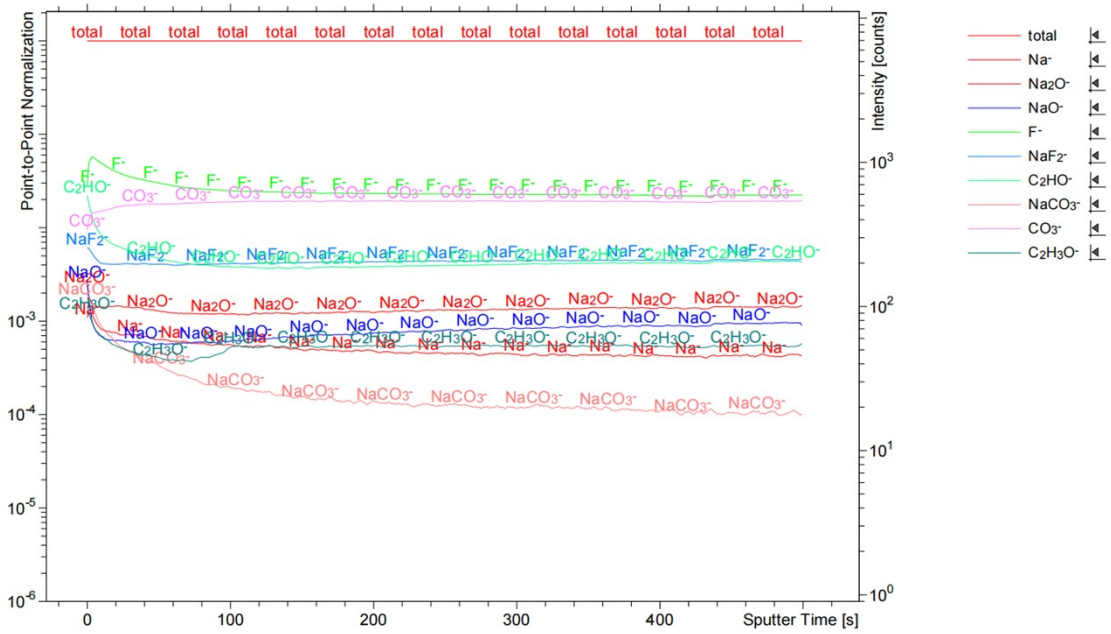

Fig. S21 Sputtering profiles of selected species in the HC anode using DEC electrolyte from the TOF-SIMS tests.

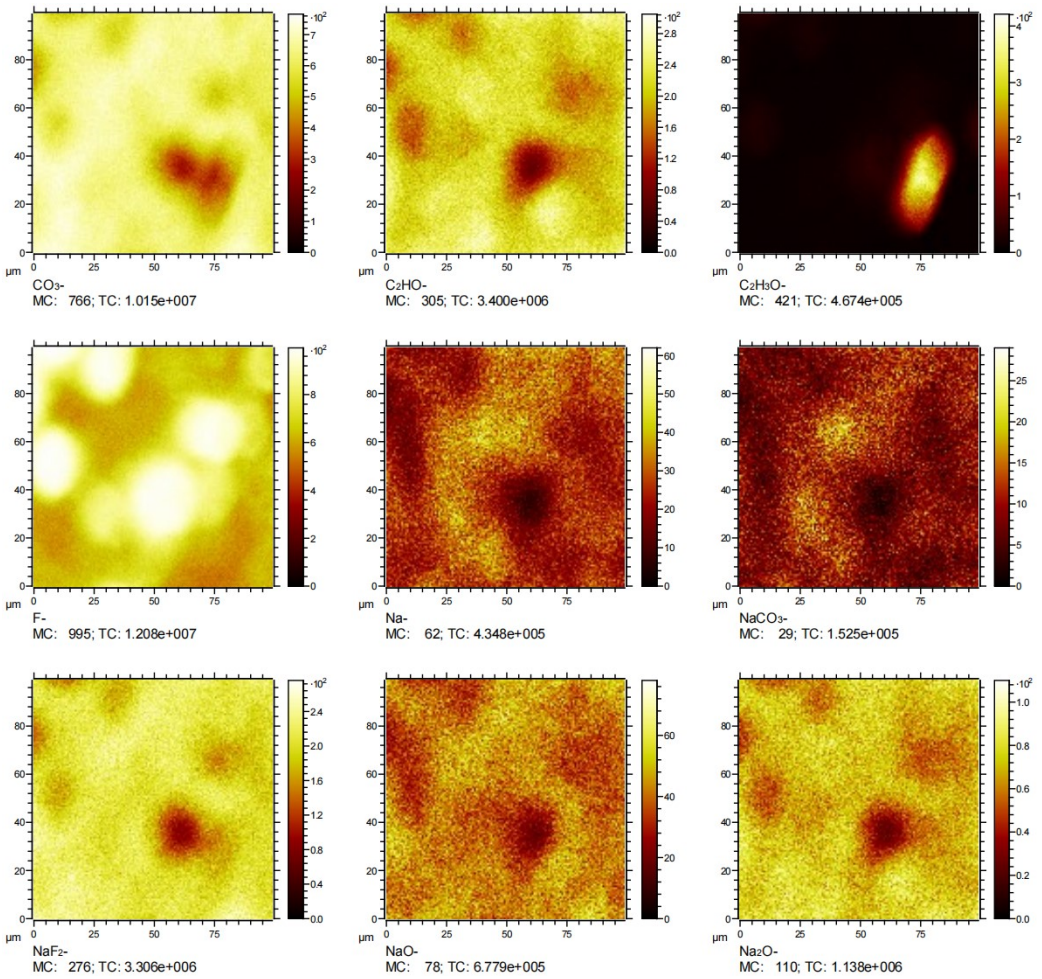

Fig. S22 The component mapping of selected species for DEC electrolyte.

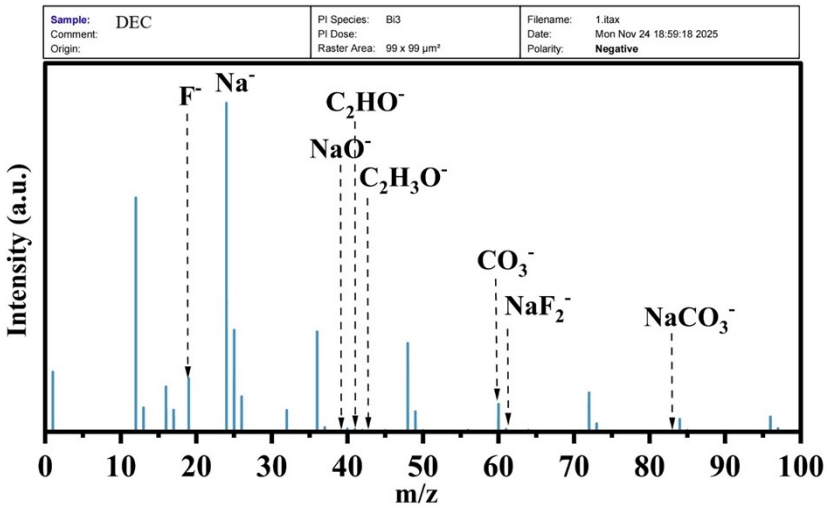

Fig. S23 The component mass spectrometry of selected species for DEC electrolyte.

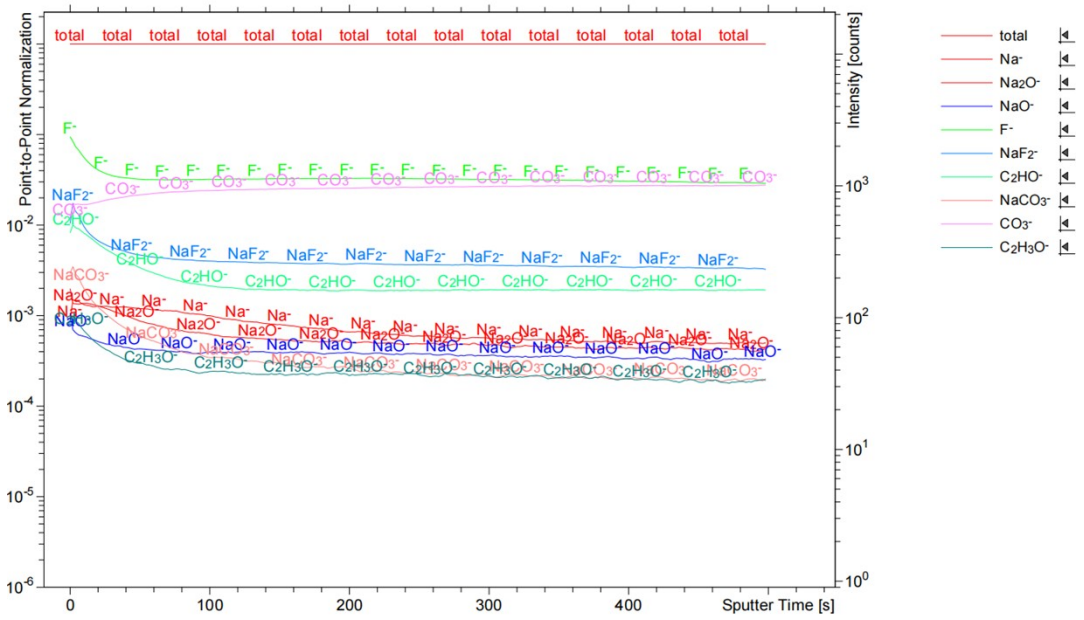

Fig. S24 Sputtering profiles of selected species in the HC anode using ETFEC electrolyte from the TOF-SIMS tests.

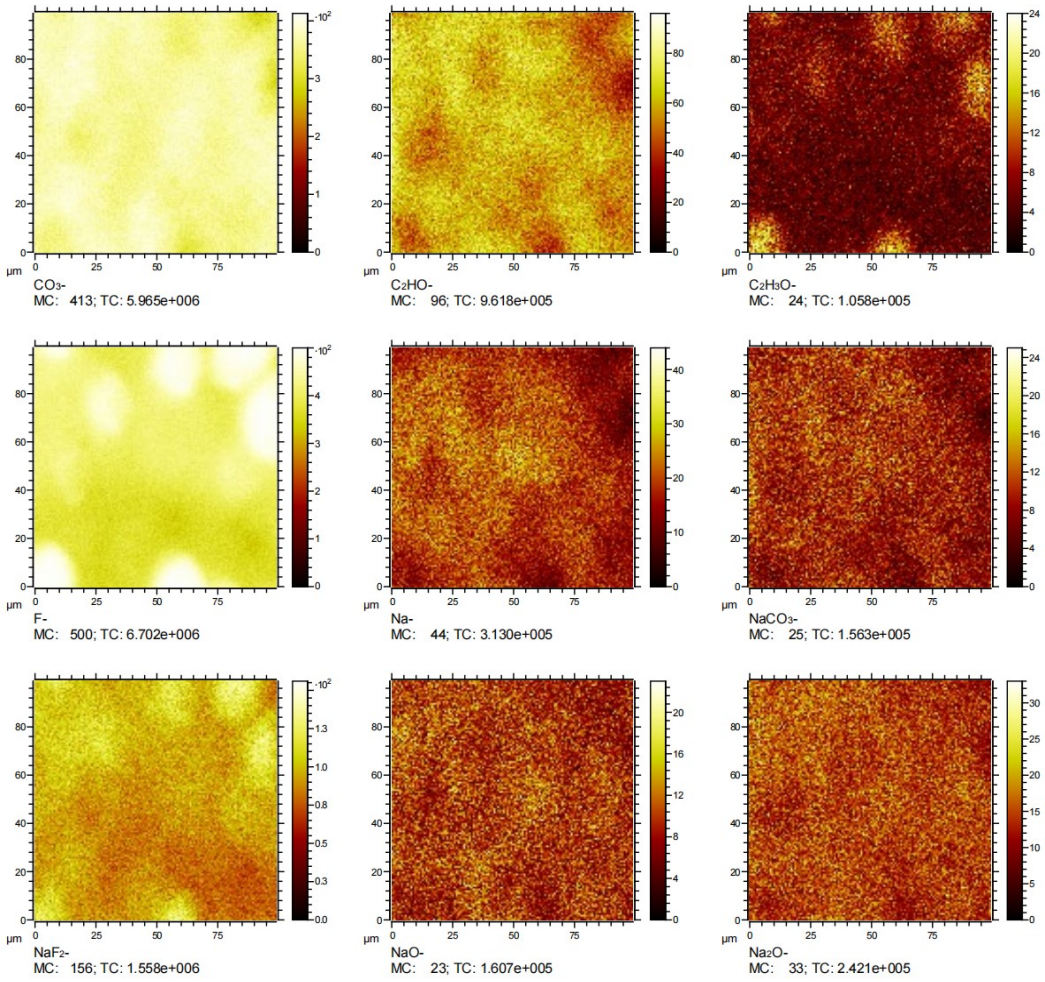

Fig. S25 The component mapping of selected species for ETFEC electrolyte.

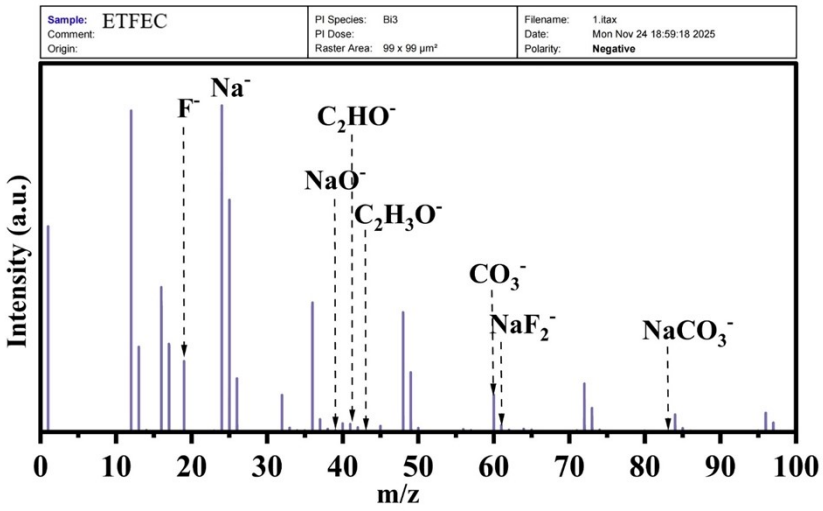

Fig. S26 The component mass spectrometry of selected species for ETFEC electrolyte.

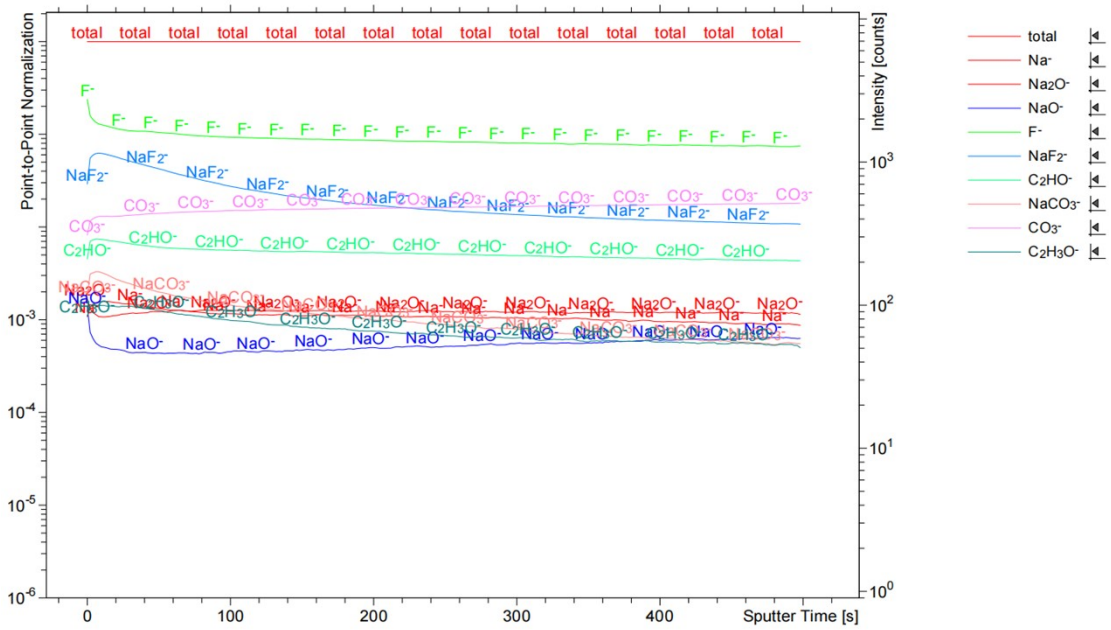

Fig. S27 Sputtering profiles of selected species in the HC anode using TFEC electrolyte from the TOF-SIMS tests.

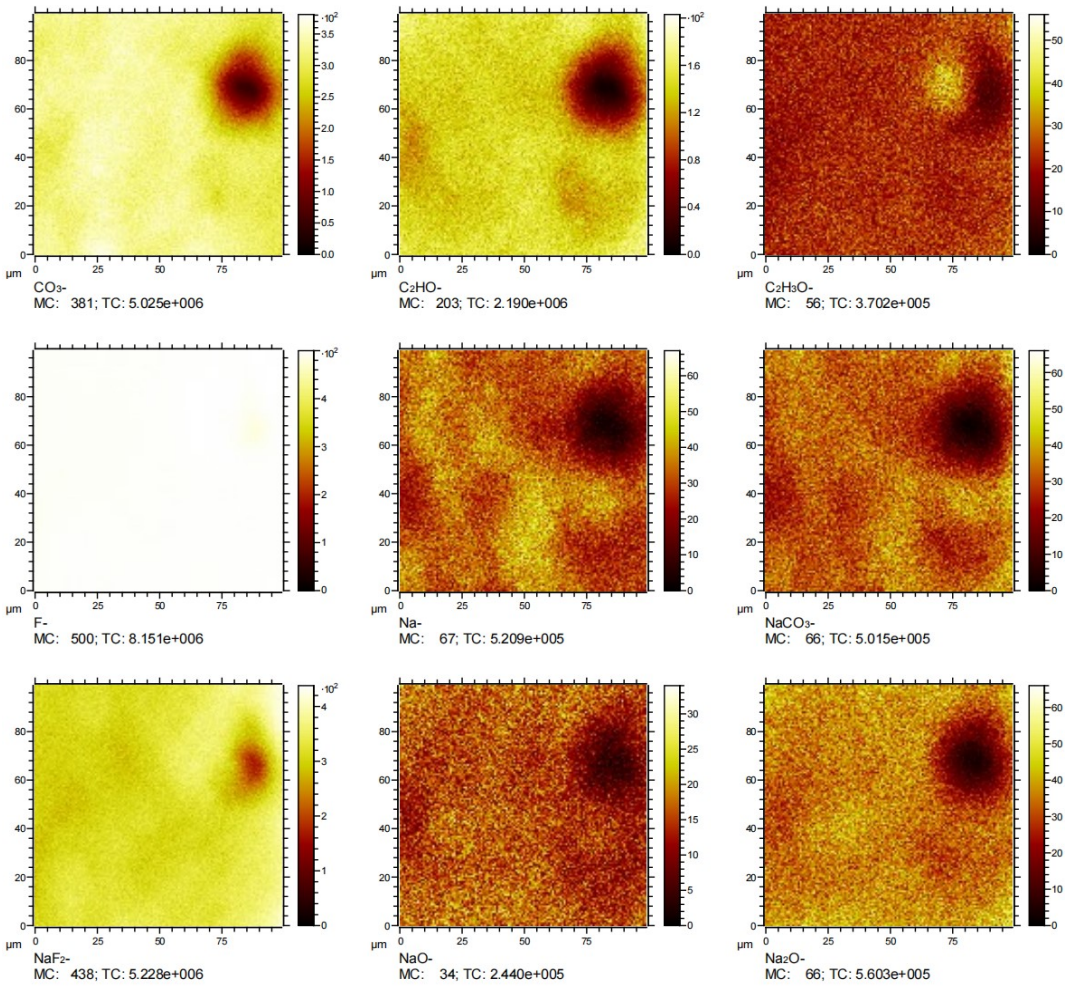

Fig. S28 The component mapping of selected species for TFEC electrolyte.

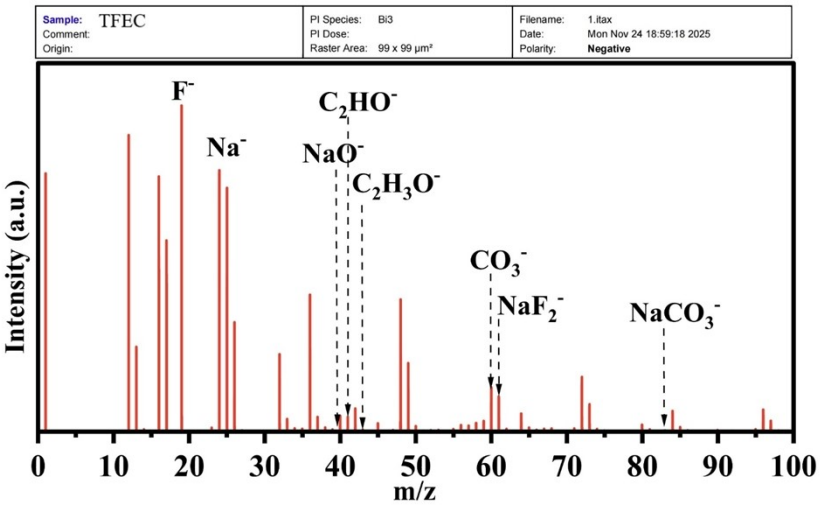

Fig. S29 The component mass spectrometry of selected species for TFEC electrolyte.

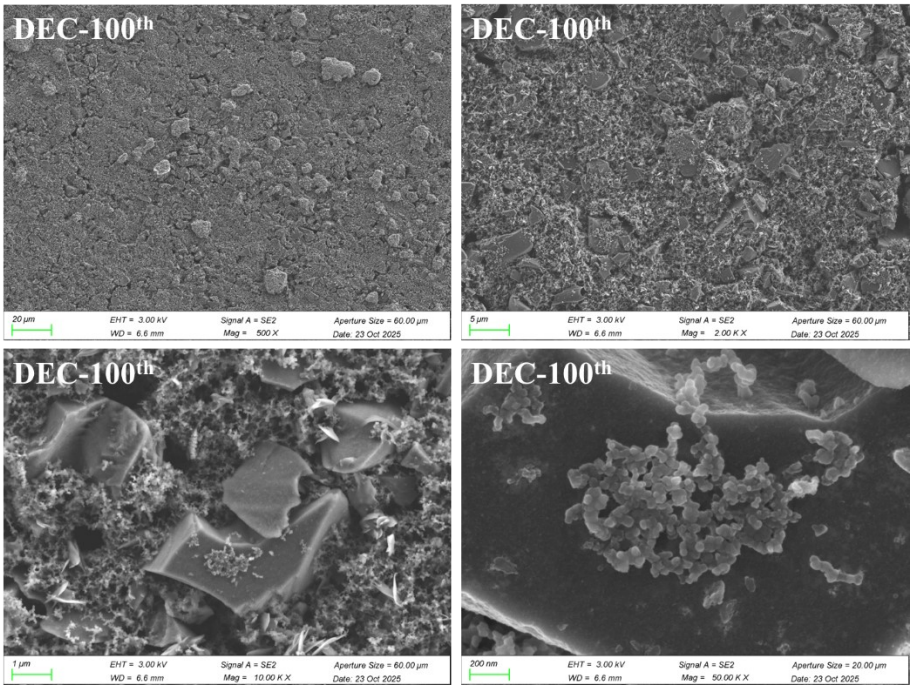

Fig. S30 SEM images of HC surface after 100 cycles in DEC electrolyte.

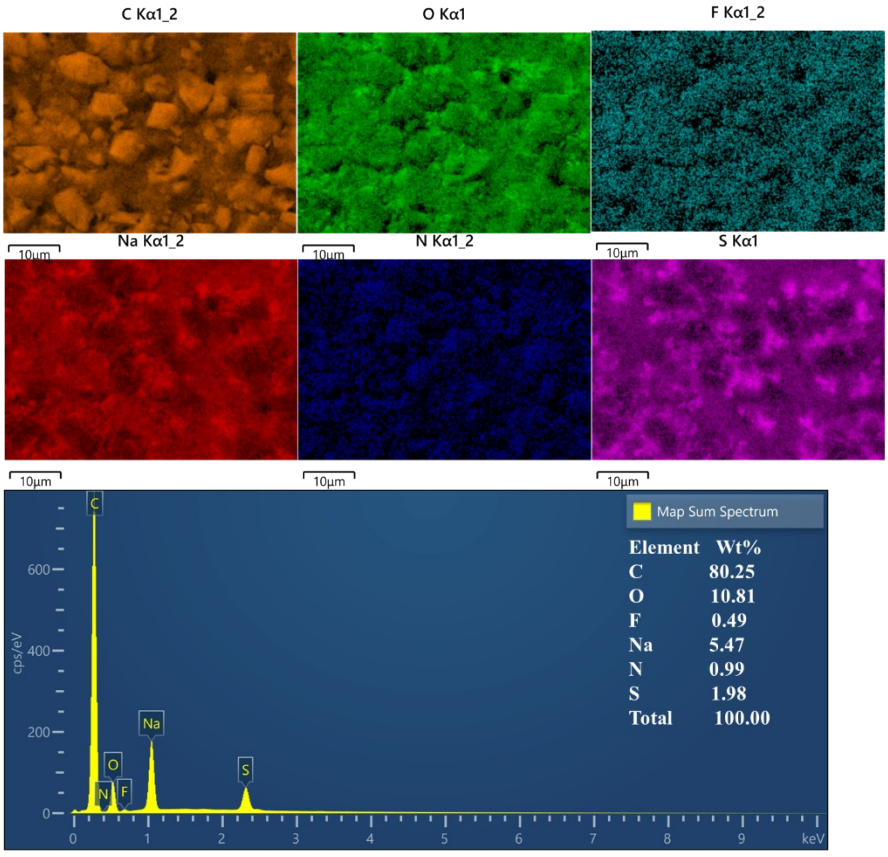

Fig. S31 EDS elemental mapping and their quantitative ratios of HC surface after 100 cycles in DEC electrolyte.

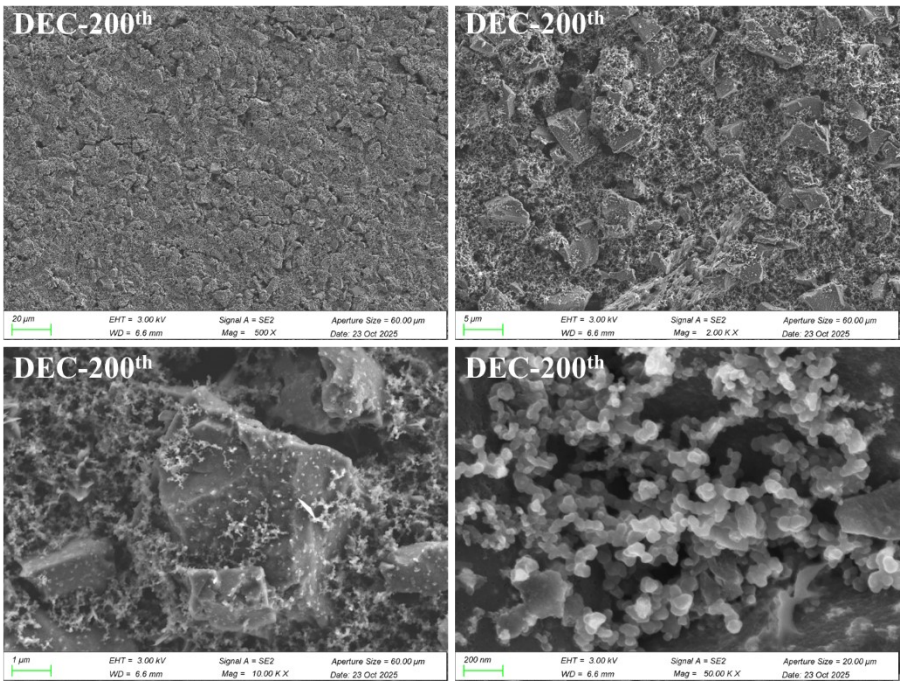

Fig. S32 SEM images of HC surface after 200 cycles in DEC electrolyte.

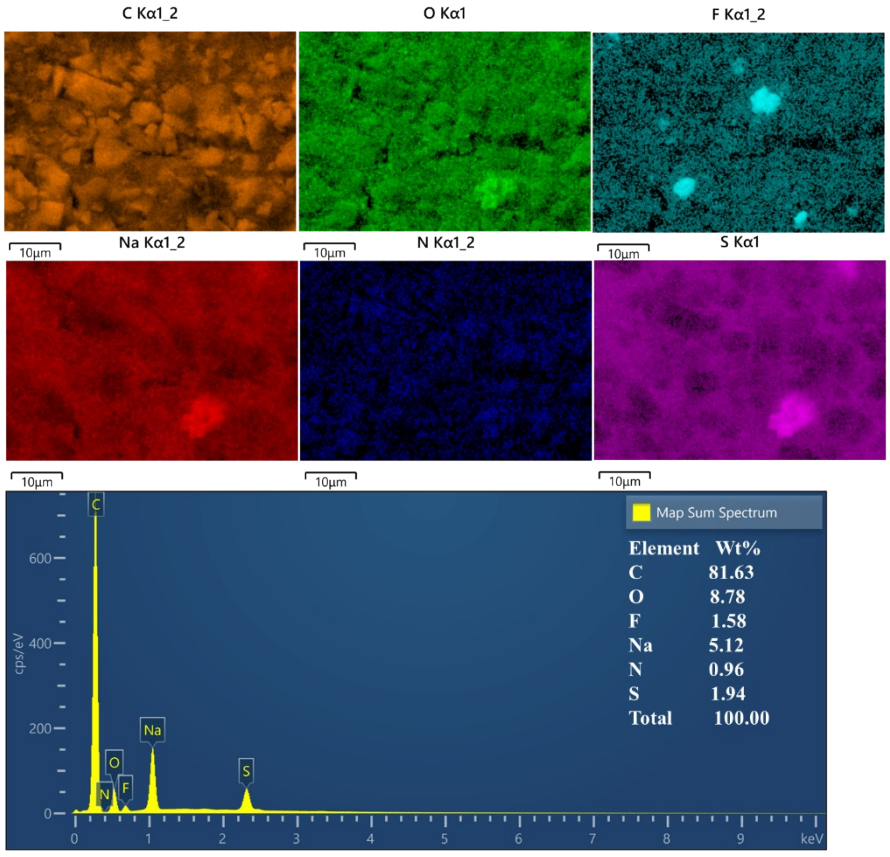

Fig. S33 EDS elemental mapping and their quantitative ratios of HC surface after 200 cycles in DEC electrolyte.

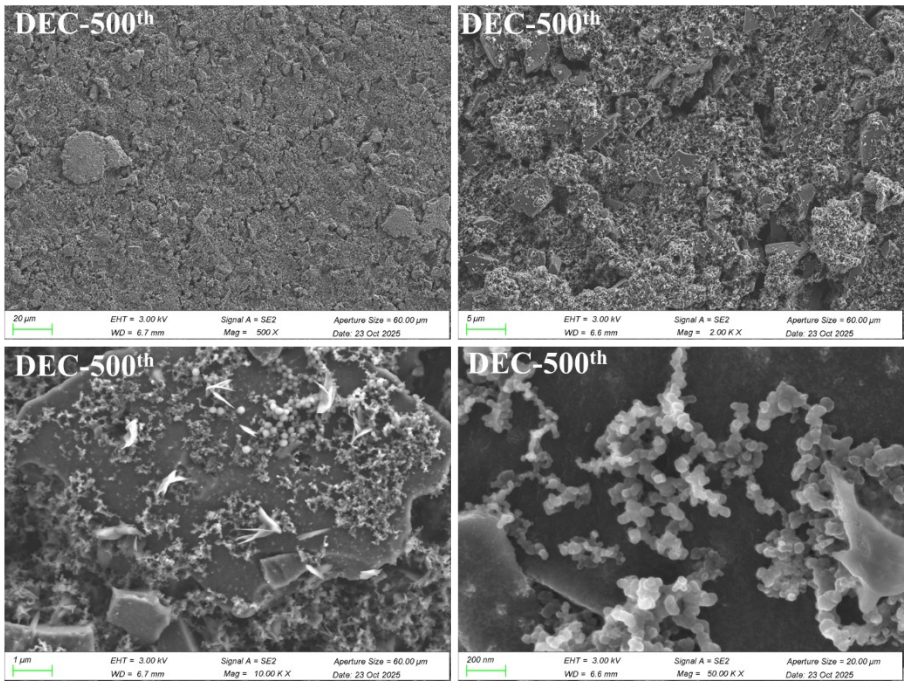

Fig. S34 SEM images of HC surface after 500 cycles in DEC electrolyte.

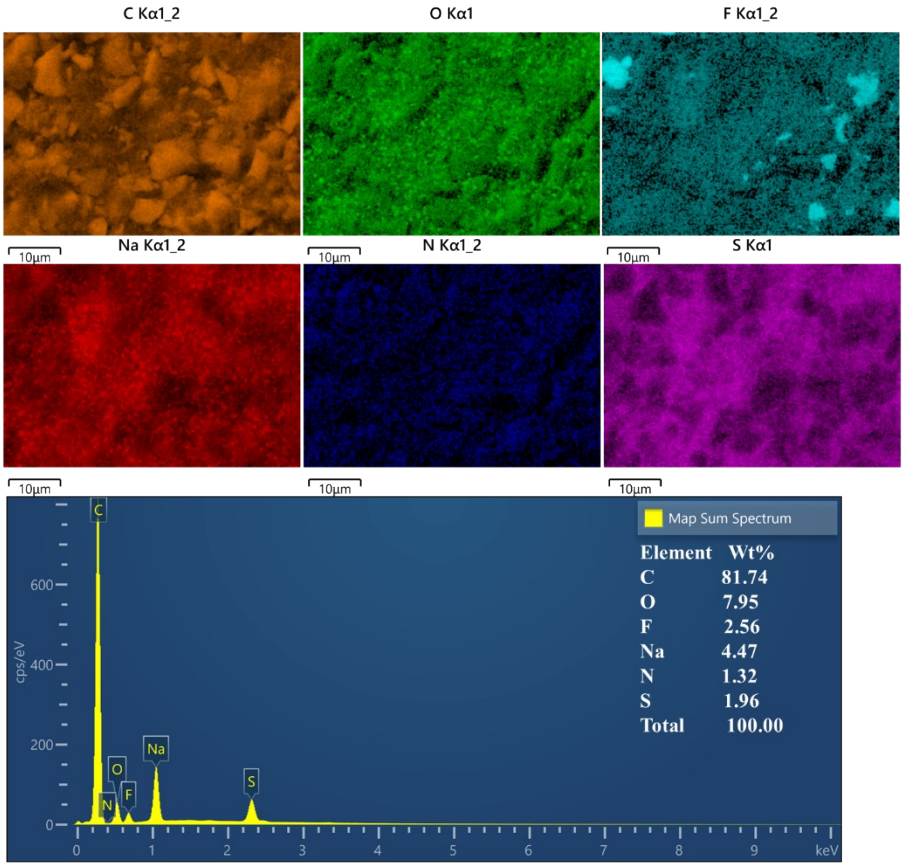

Fig. S35 EDS elemental mapping and their quantitative ratios of HC surface after 500 cycles in DEC electrolyte.

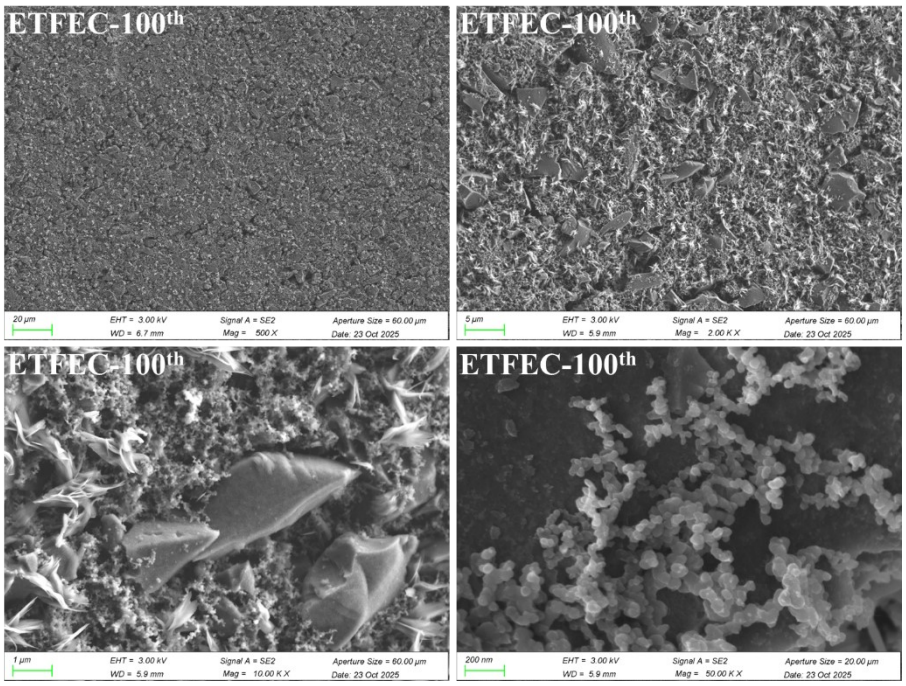

Fig. S36 SEM images of HC surface after 100 cycles in ETFEC electrolyte.

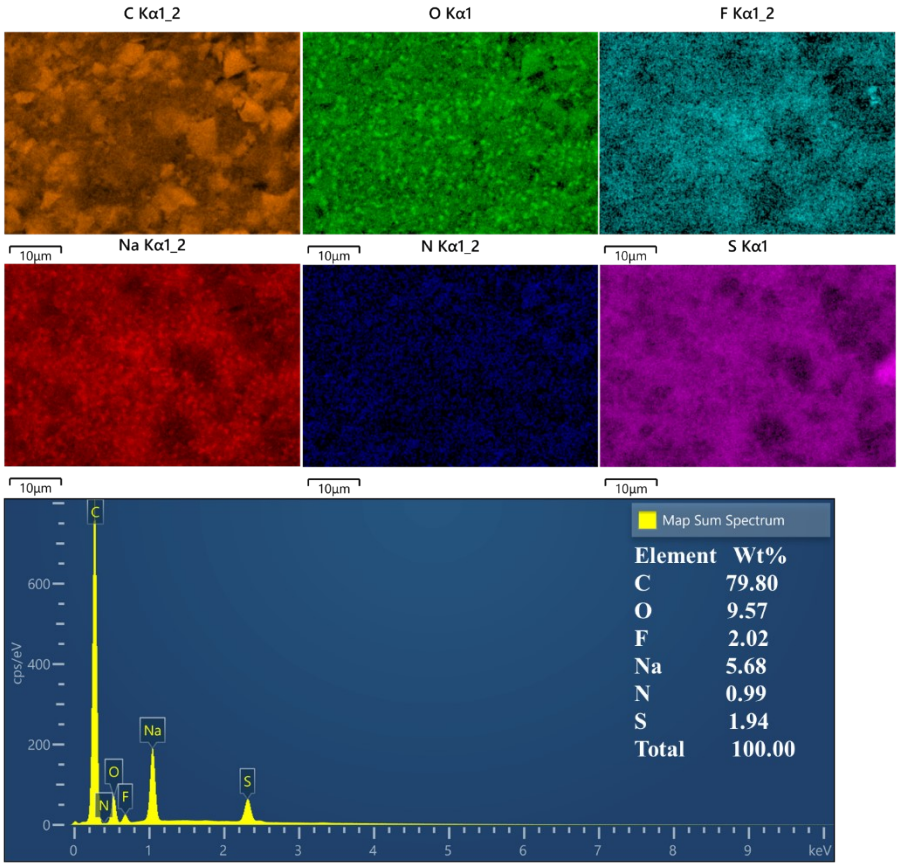

Fig. S37 EDS elemental mapping and their quantitative ratios of HC surface after 100 cycles in ETFEC electrolyte.

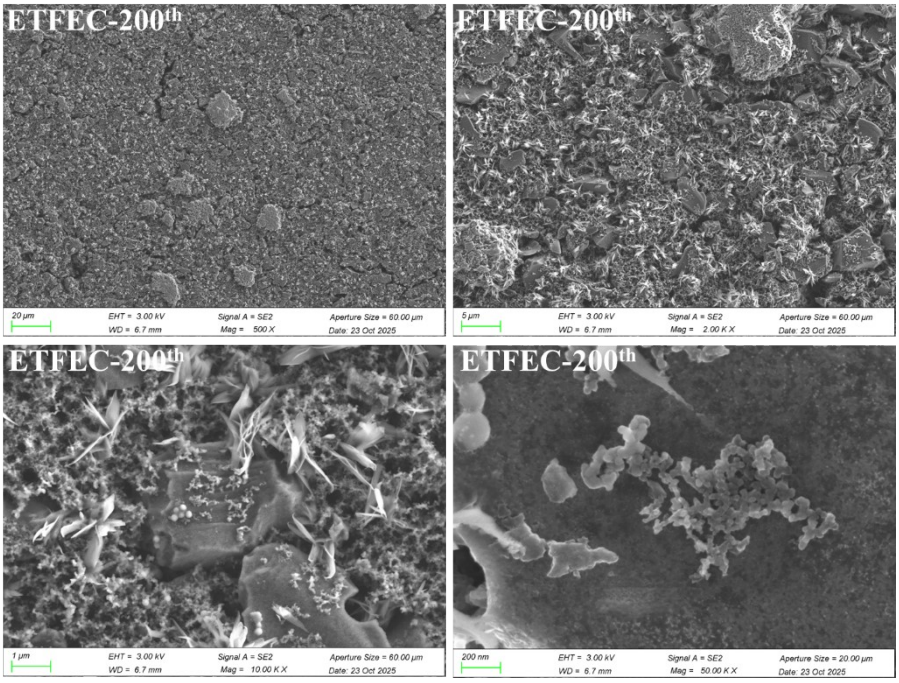

Fig. S38 SEM images of HC surface after 200 cycles in ETFEC electrolyte.

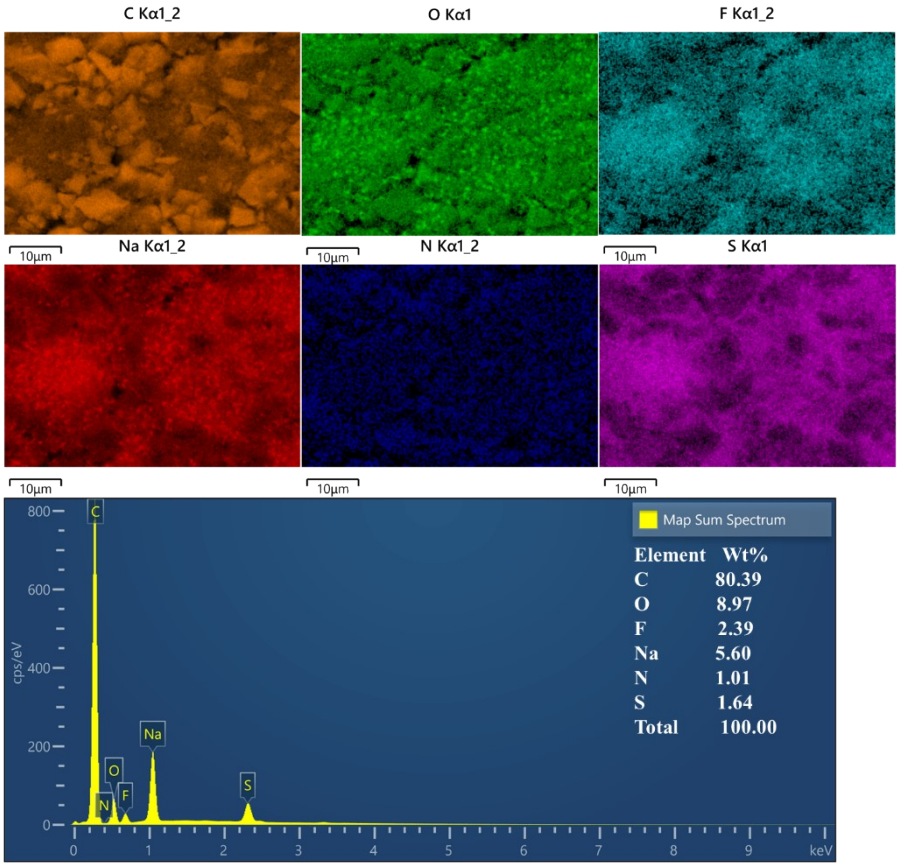

Fig. S39 EDS elemental mapping and their quantitative ratios of HC surface after 200 cycles in ETFEC electrolyte.

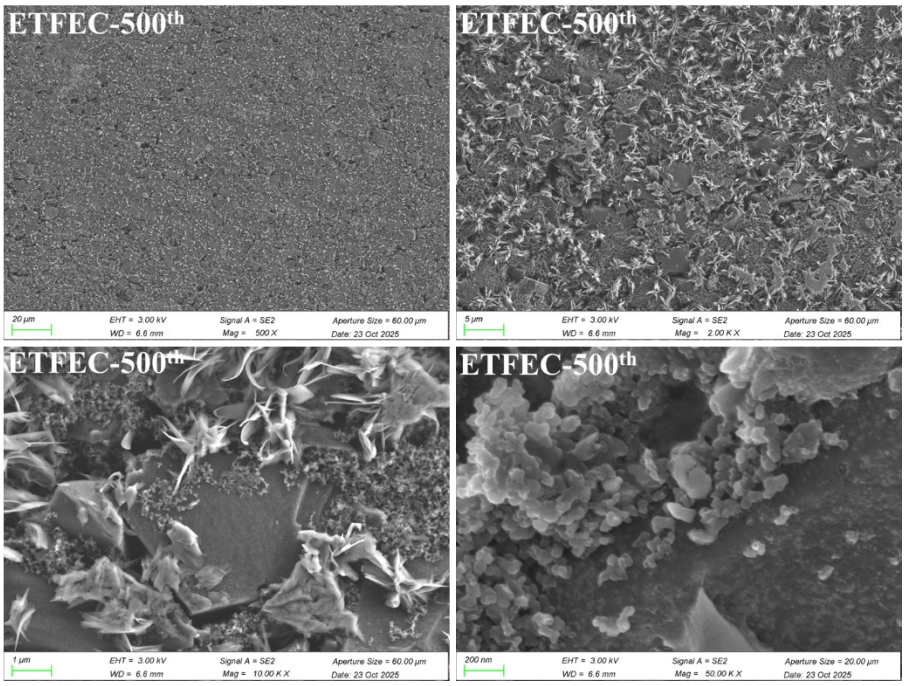

Fig. S40 SEM images of HC surface after 500 cycles in ETFEC electrolyte.

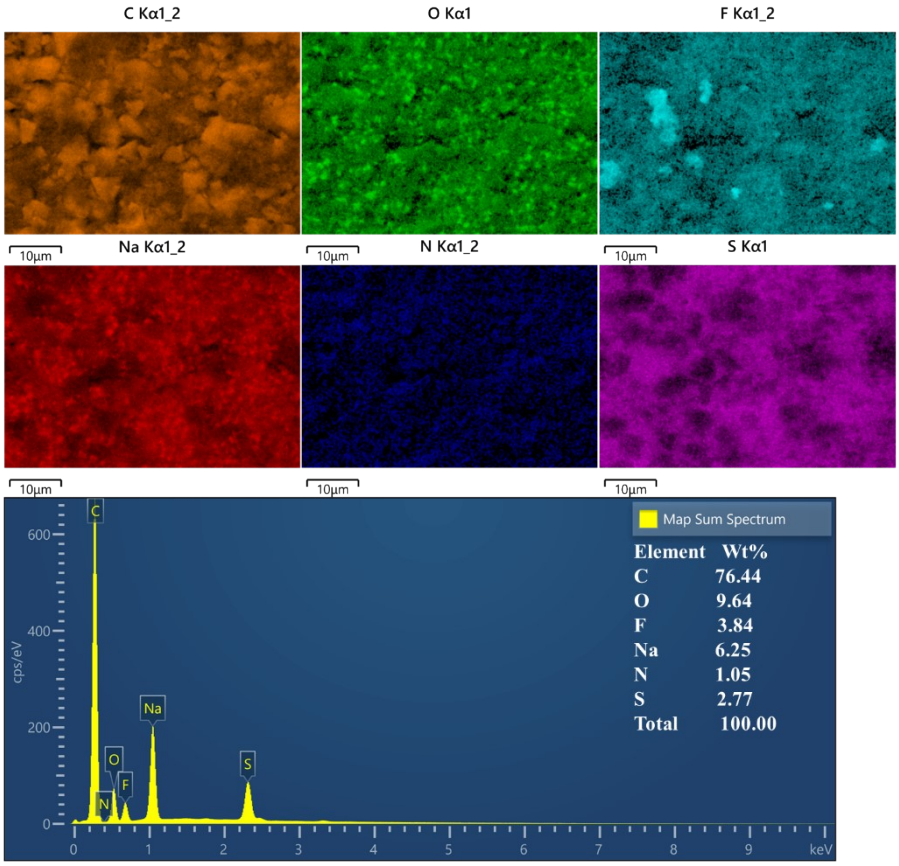

Fig. S41 EDS elemental mapping and their quantitative ratios of HC surface after 500 cycles in ETFEC electrolyte.

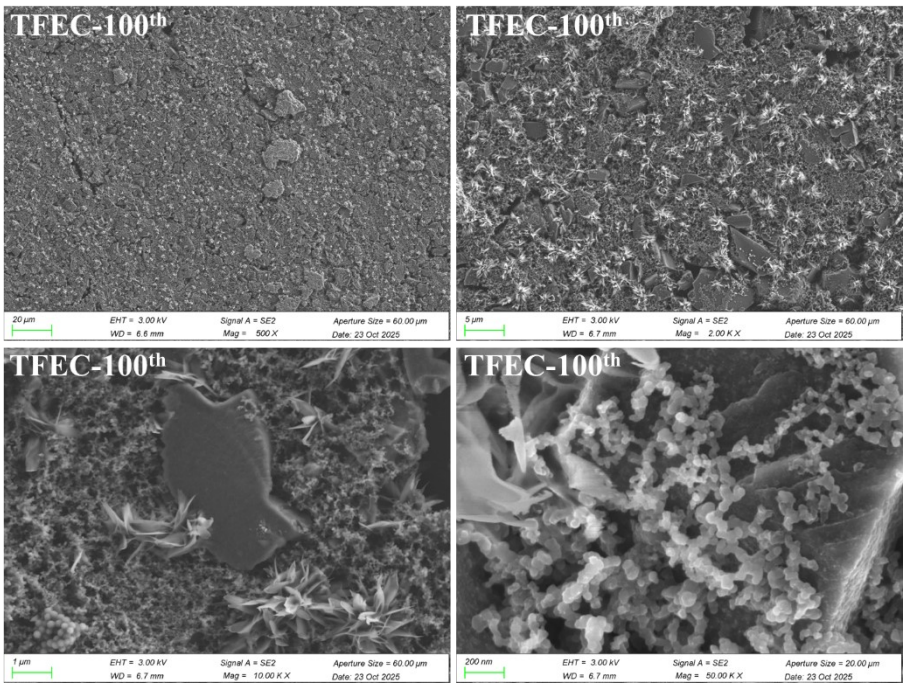

Fig. S42 SEM images of HC surface after 100 cycles in TFEC electrolyte.

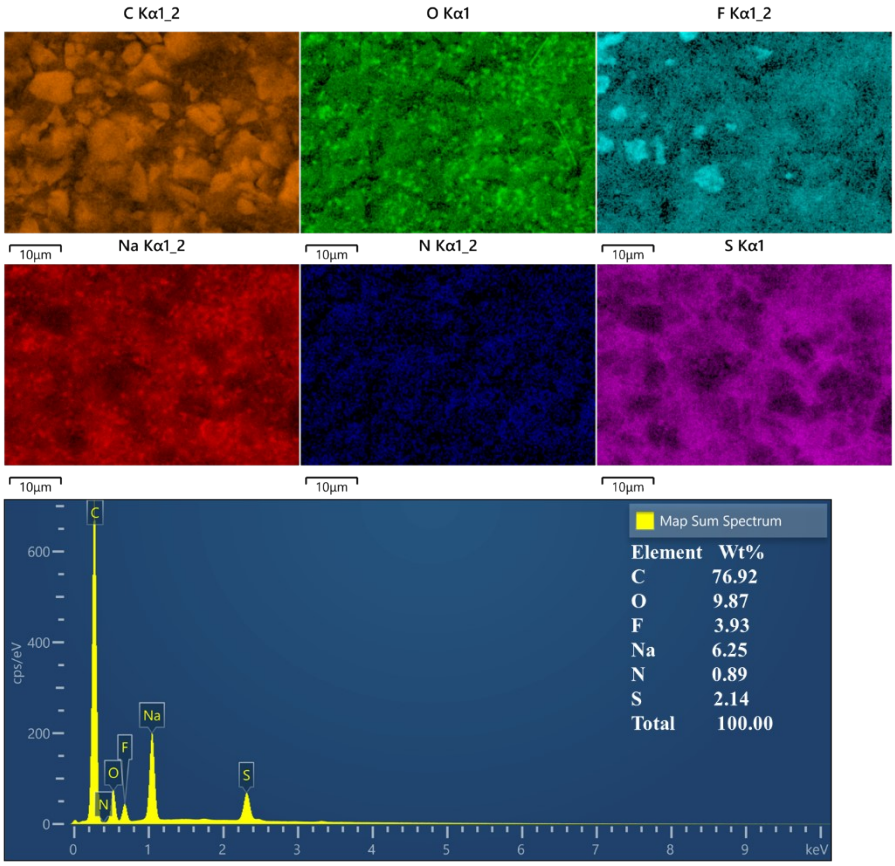

Fig. S43 EDS elemental mapping and their quantitative ratios of HC surface after 100 cycles in TFEC electrolyte.

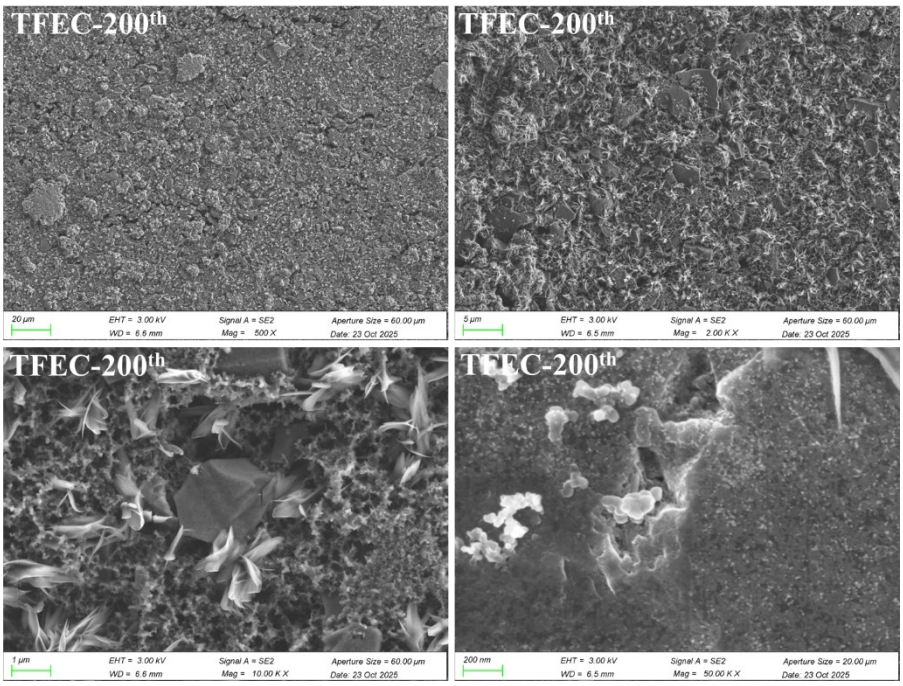

Fig. S44 SEM images of HC surface after 200 cycles in TFEC electrolyte.

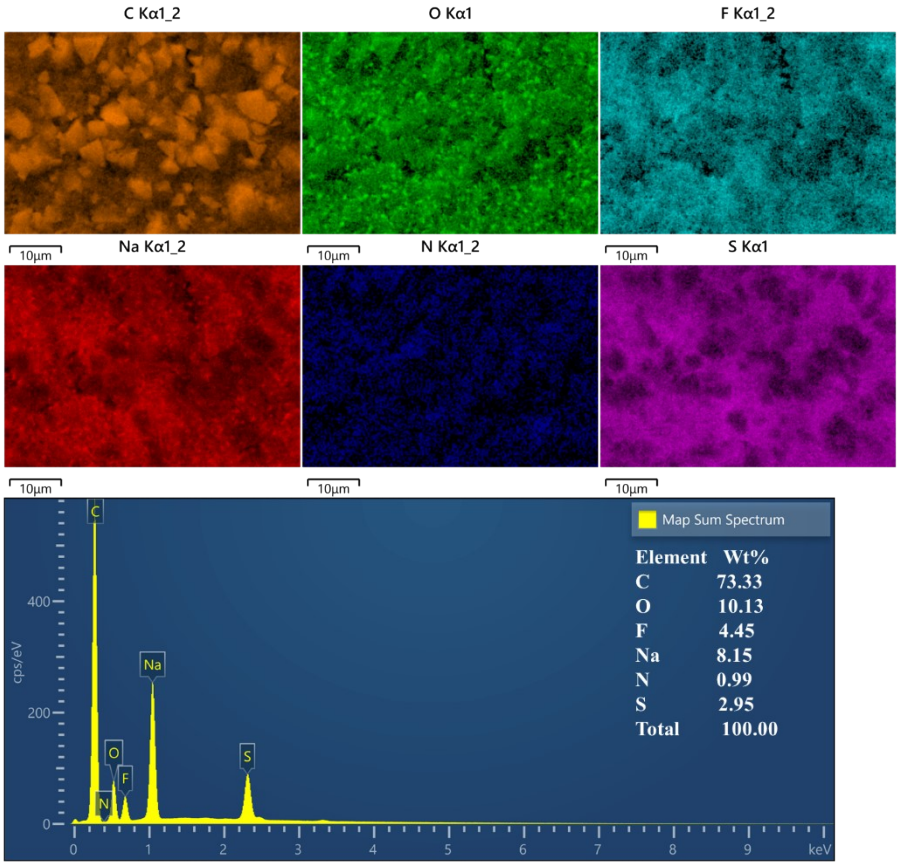

Fig. S45 EDS elemental mapping and their quantitative ratios of HC surface after 200 cycles in TFEC electrolyte.

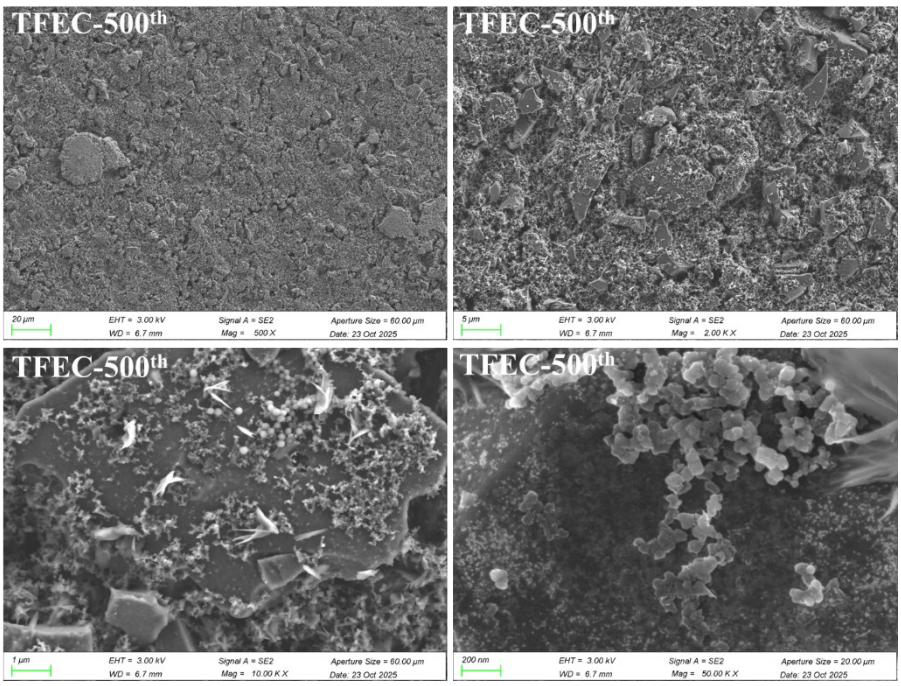

Fig. S46 SEM images of HC surface after 500 cycles in TFEC electrolyte.

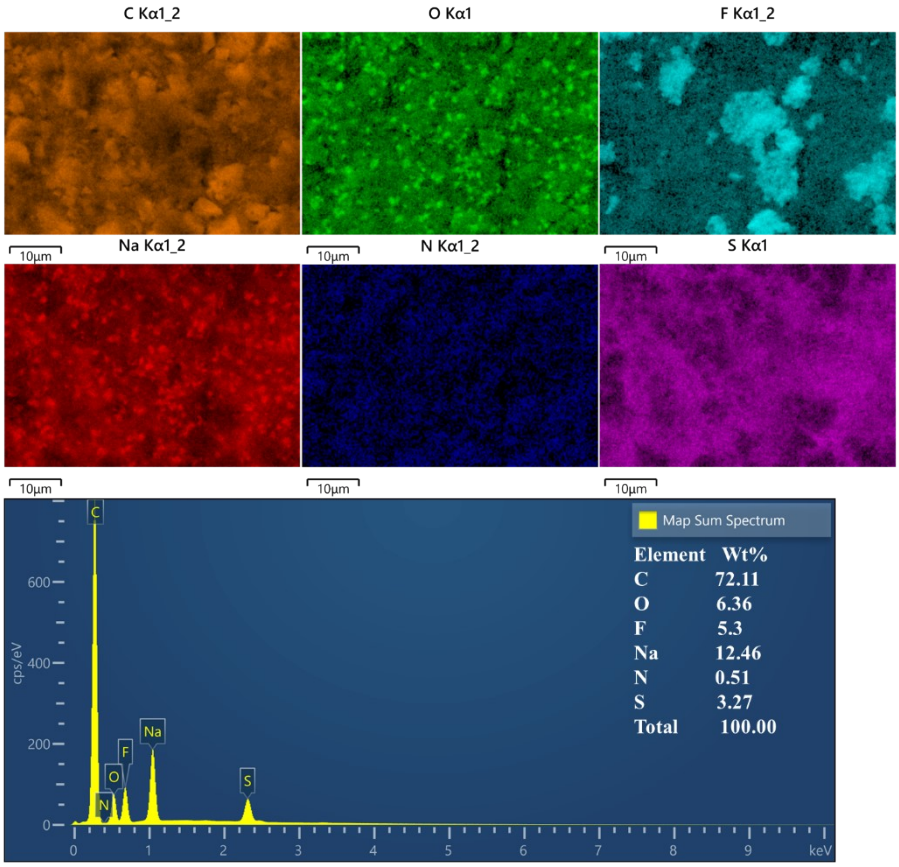

Fig. S47 EDS elemental mapping and their quantitative ratios of HC surface after 500 cycles in TFEC electrolyte.

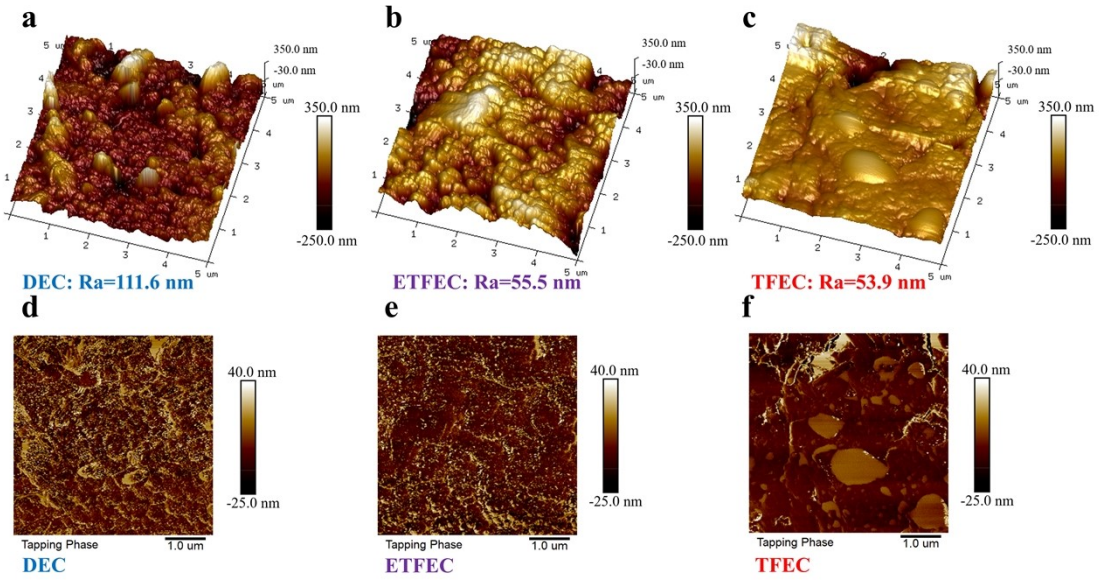

Fig. S48 The surface roughness and 3 D topography analysis of cycled electrodes with different electrolytes.

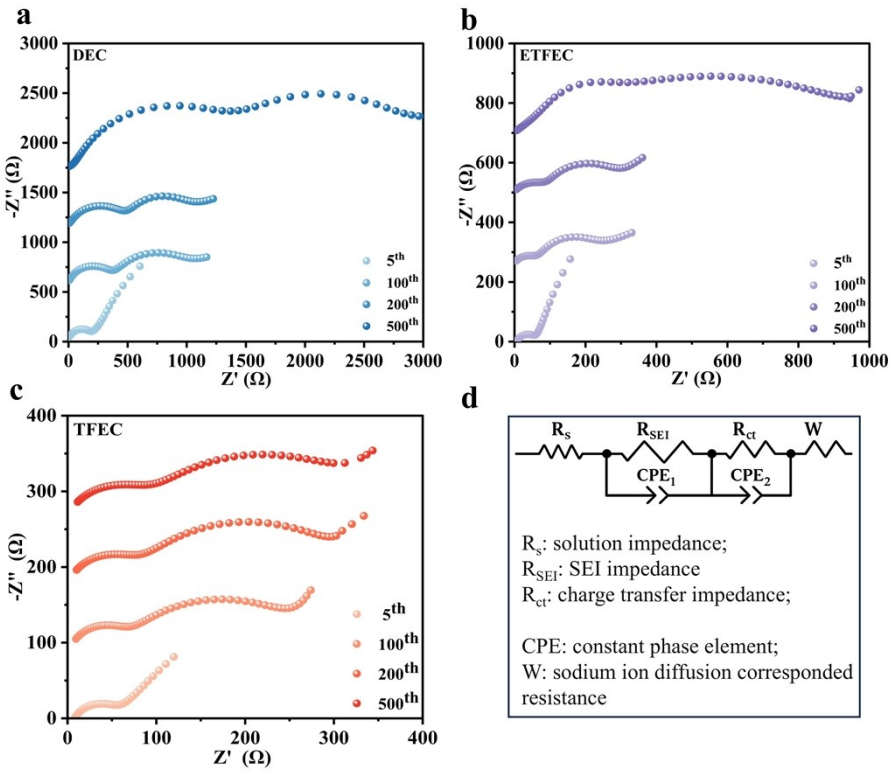

Fig. S49 The electrochemical impedances of (a) DEC, (b) ETFEC and (C) TFEC electrolytes after various cycle numbers at 0.5 A g^{-1}.

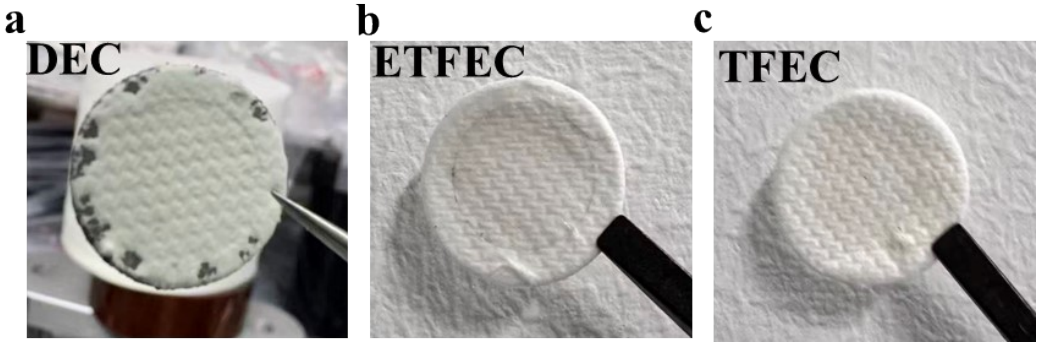

Fig. S50 Morphology of the separator surface of (a) DEC, (b) ETFEC and (C) TFEC electrolytes after 500 cycles numbers at 0.5 A g^{-1}.

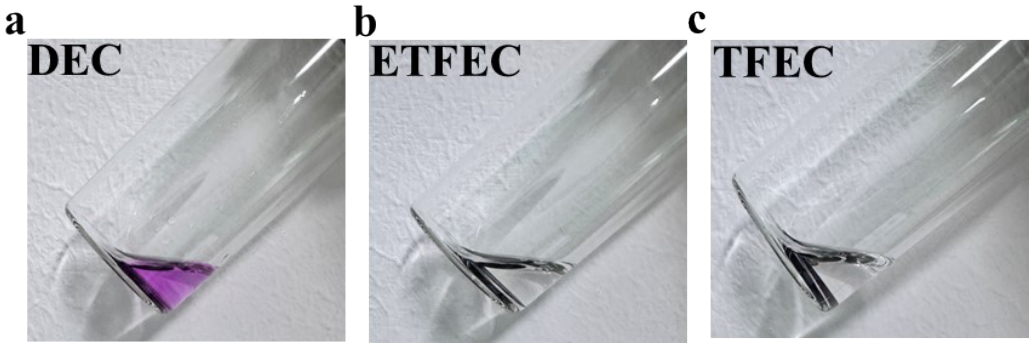

Fig. S51 Appearance of HC electrodes in phenolphthalein indicator after 500 cycles at 0.5 A g^{-1} with different electrolytes.

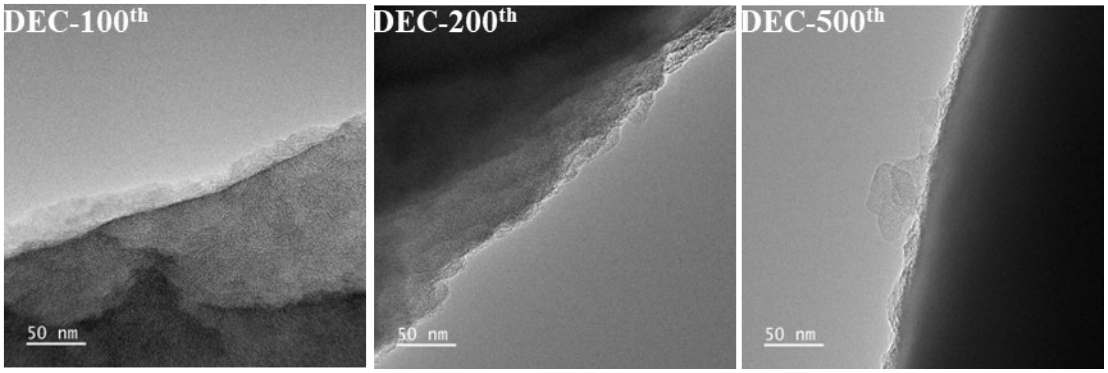

Fig. S52 High-resolution TEM images of SEI on cycled HC after 100th, 200th and 500th in DEC electrolyte.

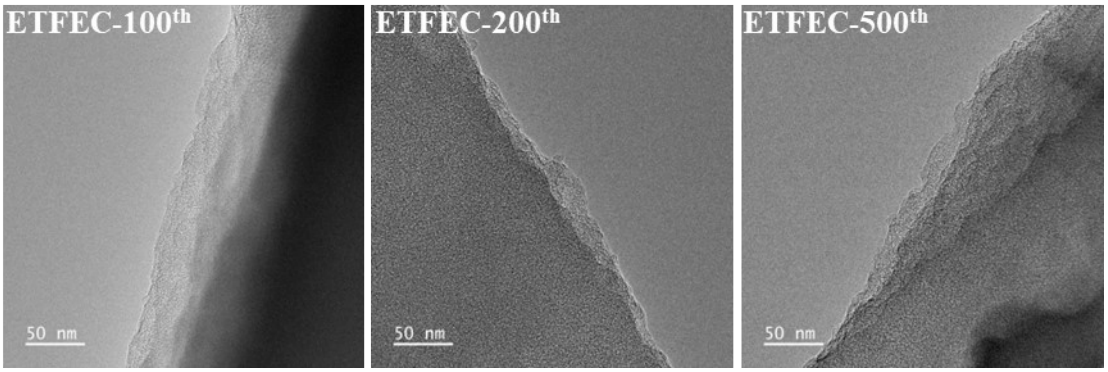

Fig. S53 High-resolution TEM images of SEI on cycled HC after 100th, 200th and 500th in ETFEC electrolyte.

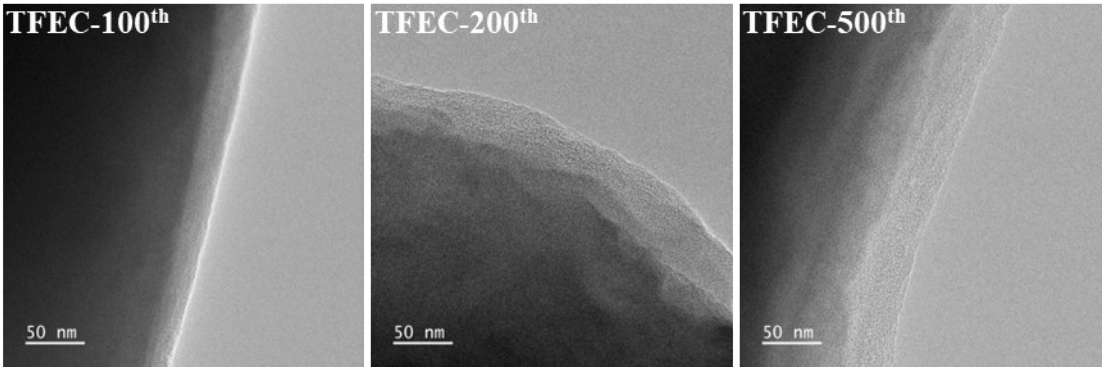

Fig. S54 High-resolution TEM images of SEI on cycled HC after 100th, 200th and 500th in TFEC electrolyte.

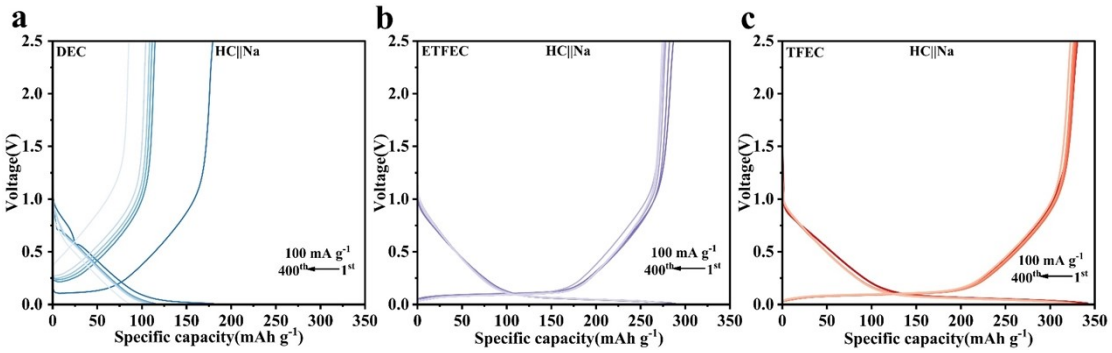

Fig. S55 The corresponding discharging/charging curves of HC||Na cells at 0.1 A g^{-1} using DEC, ETFEC and TFEC electrolytes.

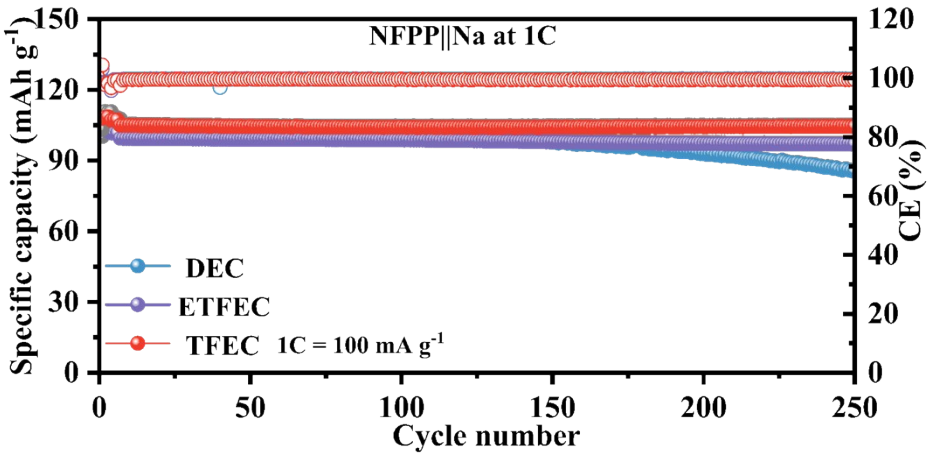

Fig. S56 Cycling performance of NFPP||Na cells using DEC, ETFEC and TFEC electrolytes at 1C.

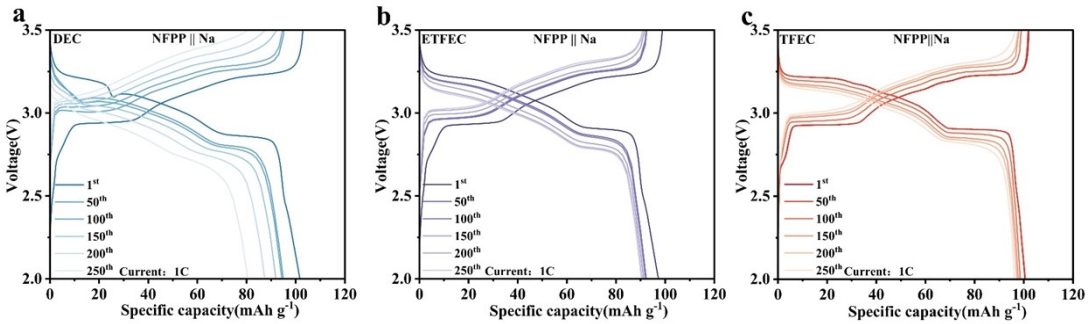

Fig. S57 The charge-discharge curves of NFPP||Na cells using DEC, ETFEC, TFEC electrolytes.

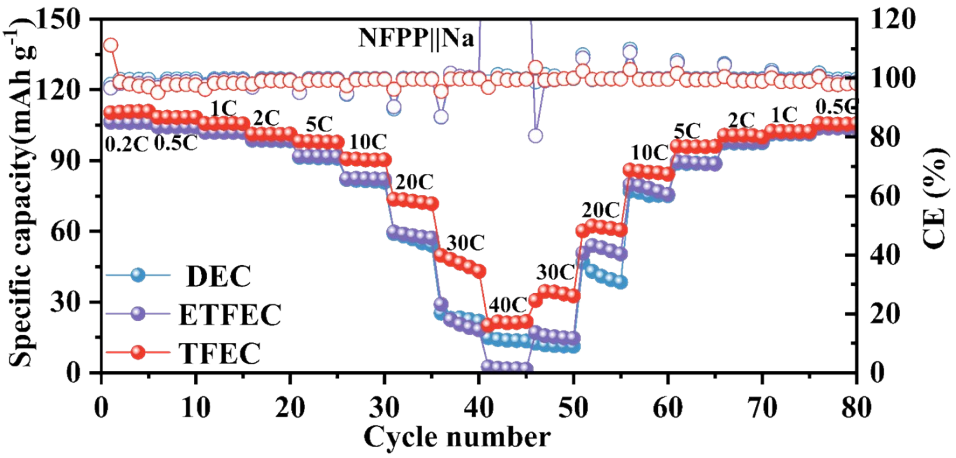

Fig. S58 Rate capability of NFPP||Na cells using DEC, ETFEC and TFEC electrolytes.

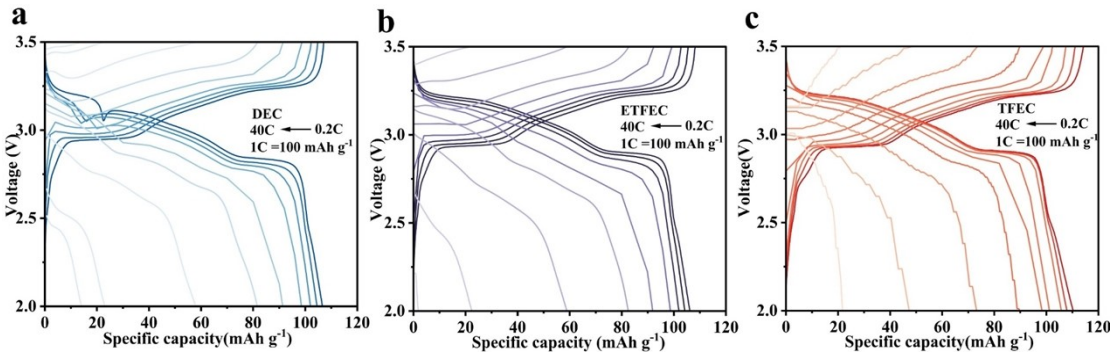

Fig. S59 The charge-discharge curves of NFPP||Na cells using DEC, ETFEC, TFEC electrolytes.

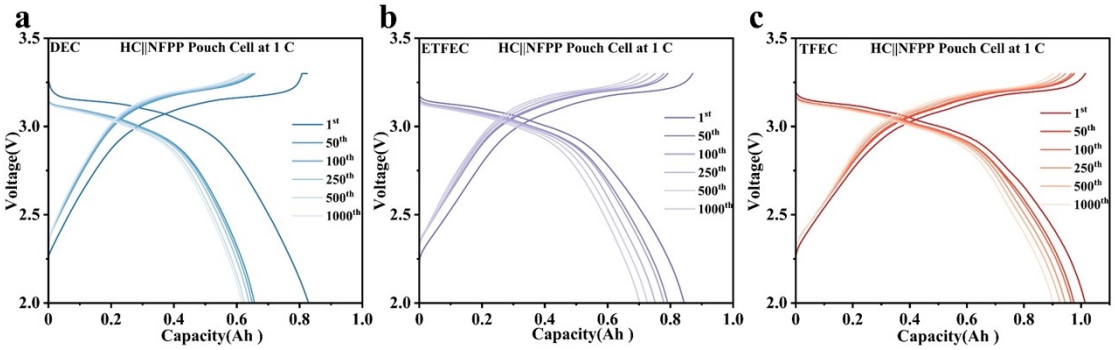

Fig. S60 The charge-discharge curves of HC||NFPP pouch cells using DEC, ETFEC, TFEC electrolytes.

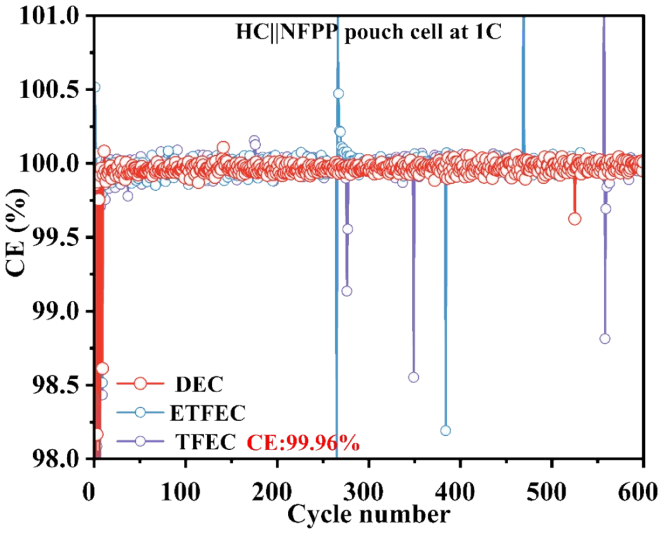

Fig. S61 Coulombic efficiency of HC||NFPP pouch cells with DEC, ETFEC and TFEC electrolytes.

Table S1. The comparison of different electrolyte design strategies.

Electrolyte type	**Solvation structure**	**Conductivity**	**SEI type**	**Advantages**	**Limitations**
HCE / LHCE	Anion-dominated (high CIP/AGG)	Low-moderate	Inorganic-rich	Stable SEI	High viscosity, high cost
Weakly solvating	Weak Na^+-solvent interaction	Low-moderate	Moderately inorganic	Fast desolvation	Low conductivity
Fluorinated (literature)	Partially anion-enriched	Moderate	Mixed SEI (more NaF)	Improved stability	Increased cost/viscosity
This work (TFEC)	Anion-enriched at low salt	High (~10 mS cm^{-1})	Thin inorganic-rich (NaF/Na_2CO_3)	Fast kinetics + high conductivity	Sustainability concerns

Table S2. Physical and chemical properties of several electrolytic solvents.

Name	Dielectric Constant	Viscosity ($\times10^{-3}$ Pa·s)	Melting Point (℃)	Boiling Point (℃)	Number of Donors
Ethylene Carbonate (EC)	89.78	1.99	36.4	248	16.4
Dimethyl Carbonate (DMC)	3.09	0.58	4.6	91	16.0
Diethyl Carbonate (nonF-DEC)	2.82	0.75	-73	126	16.0
Ethyl(2,2,2-trifluoroethyl)carbonate (semF-DEC)	/	/	/	102.5	/
Tri (trifluoroethyl) carbonate (fulF-DEC)	/	/	/	118	/

Table S3. The composition of different electrolytes.

Name	Electrolytes Composition	Content of H_2O (ppm)
DEC	1 M NaFSI + EC + DMC + nonF-DEC (25:65:10, Vol)	13.3 ppm
ETFEC	1 M NaFSI + EC + DMC + semF-DEC (25:65:10, Vol)	9.0 ppm
TFEC	1 M NaFSI + EC + DMC + fulF-DEC (25:65:10, Vol)	16.6 ppm

Table S4. The fabrication parameters of 1 Ah HC||NFPP pouch cells.

Cell capacity (Ah)	1	
Cathode	Active material	$Na_4Fe_3(PO_4)_2P_2O_7$ (NFPP)
	Active material percentage (wt%)	95.1
	Area weight (each side, mg cm^{-2})	29.5
	Length (mm)	80
	Width (mm)	50
	Thickness (μm)	181
	Compact density (g cm^{-3})	1.6
Anode	Active materials	Hard Carbon
	Active material percentage (wt%)	92.5
	Area weight (each side, mg cm^{-2})	11.1
	Length (mm)	80
	Width (mm)	50
	Thickness (μm)	140
	Compact density (g cm^{-3})	0.8
Layer of cathodes	5	
Layer of anodes	6	
Negative to positive capacity ratio		1.2
Electrolyte to capacity ratio (g Ah^{-1})		9.0

Table S5. The full charging protocol of 1 Ah HC||NFPP pouch cells and 52 Ah prismatic cell.

Full charging protocol	
Formation steps at 45°C under clamping pressure (75 kPa)	1. Rest for 5 min 2. 0.05C CC charge for 3 h; 3. Rest for 5 min 4. 0.2C CC–CV charge to 3.5 V (cut-off current: 0.05C) 5. Rest for 5 min 6. 0.05C discharge to 2.0 V 7. 0.2C CC–CV charge to 3.5 V 8. 0.2C discharge to 2.0 V
Aging (25°C)	Rest for 24 h
Grading (25°C)	1. 0.2C CC–CV charge to 3.5 V (cut-off current: 0.05C) 2. Rest for 5 min 3. 0.2C discharge to 2.0 V
Cycling (25°C)	1. 1C CC charge to 3.3 V 2. Rest for 5 min 3. 1C discharge to 2.0 V 4. Rest for 5 min

References

[1] Wang, X. *et al.* Anion/cation solvation engineering for a ternary low-concentration electrolyte toward high-voltage and long-life sodium-ion batteries. *Adv. Funct. Mater.* **34**, 2315007 (2024).

[2] Dai, H. *et al*. Mechanistic understanding of a bifunctional carbonate additive for enhanced performance in lithium-sulfur battery. *Energy Storage Mater.* **76,** 104123 (2025).

[3] Zhou, X. *et al.* Anion-reinforced solvation for a gradient inorganic-rich interphase enables high-rate and stable sodium batteries. *Angew. Chem. Int. Ed.* **61**, e202205045 (2022).

[4] Pronk, S. et al. GROMACS 4.5: a high-throughput and highly parallel open source molecular simulation toolkit. *Bioinformatics* 29, 845–854 (2013).

[5] Grimme, S., Antony, J., Ehrlich, S. & Krieg, H. A consistent and accurate Ab initio parametrization of density functional dispersion correction (DFT-D) for the 94 elements H-Pu. *J. Chem. Phys.* 132, 154104 (2010).

[6] Krishnan, R., Binkley, J. S., Seeger, R. & Pople, J. A. Self-consistent molecular orbital methods. XX. a basis set for correlated wave functions. *J. Chem. Phys.* 72, 650–654 (1980).

[7] Frisch, M. J., Pople, J. A. & Binkley, J. S. Self-consistent molecular orbital methods 25. supplementary functions for gaussian basis sets. *J. Chem. Phys.* 80, 3265–3269 (1984).

[8] Clark, T., Chandrasekhar, J., Spitznagel, G. W. & Schleyer, P. V. R. Efficient diffuse function-augmented basis sets for anion calculations. III. The 3-21+G basis set for first-row elements, Li-F. *J. Comput. Chem.* 4, 294–301 (1983).

[9] Abraham, M. J. et al. GROMACS: high performance molecular simulations through multi-level parallelism from laptops to supercomputers. *SoftwareX* 1-2, 19–25 (2015).

[10] Dodda, L. S., Vilseck, J. Z., Tirado-Rives, J. & Jorgensen, W. L. 1.14*CM1A-LBCC: localized bond-charge corrected CM1A charges for condensed-phase simulations. *J. Phys. Chem. B* 121, 3864–3870 (2017).

[11] Martínez, L., Andrade, R., Birgin, E. G. & Martínez, J. M. PACKMOL: a package for building initial configurations for molecular dynamics simulations. *J. Comput. Chem.* 30, 2157–2164 (2009).

[12] Humphrey, W., Dalke, A. & Schulten, K. VMD: visual molecular dynamics. *J. Mol. Graph.* 14, 33–38 (1996).

[13] Johnson, E. R. et al. Revealing noncovalent interactions. *J. Am. Chem. Soc.* 132, 6498–6506 (2010).

[14] Zhang, M. et al. An extended π-conjugated porous polymer with dense multiple redox centers boosts high-efficiency sodium-ion storage. *Adv. Funct. Mater.* (2025) doi:https://doi.org/10.1002/adfm.202521114.